

THE PHYSICAL ORIGIN OF LONG GAS DEPLETION TIMES IN GALAXIES

VADIM A. SEMENOV^{1,2,*}, ANDREY V. KRAVTSOV^{1,2,3} AND NICKOLAY Y. GNEDIN^{1,2,4}

To be submitted to the Astrophysical Journal

ABSTRACT

We present a model that elucidates why gas depletion times in galaxies are long compared to the time scales of the processes driving the evolution of the interstellar medium. We show that global depletion times are not set by any “bottleneck” in the process of gas evolution towards the star-forming state. Instead, depletion times are long because star-forming gas converts only a small fraction of its mass into stars before it is dispersed by dynamical and feedback processes. Thus, complete depletion requires that gas transitions between star-forming and non-star-forming states multiple times. Our model does not rely on the assumption of equilibrium and can be used to interpret trends of depletion times with the properties of observed galaxies and the parameters of star formation and feedback recipes in galaxy simulations. In particular, the model explains the mechanism by which feedback self-regulates star formation rate in simulations and makes it insensitive to the local star formation efficiency. We illustrate our model using the results of an isolated L_* -sized disk galaxy simulation that reproduces the observed Kennicutt-Schmidt relation for both molecular and atomic gas. Interestingly, the relation for molecular gas is close to linear on kiloparsec scales, even though a non-linear relation is adopted in simulation cells. This difference is due to stellar feedback, which breaks the self-similar scaling of the gas density PDF with the average gas surface density.

Subject headings: galaxies: evolution – ISM: kinematics and dynamics – stars: formation – methods: numerical

1. INTRODUCTION

One of the widely recognized basic facts about observed galaxies is that they convert gas into stars inefficiently. Star formation rates of galaxies are surprisingly low, given the total mass and density of their interstellar gas and the expected time scales of processes driving star formation.

As an example, the star formation rate (SFR) of the Milky Way (MW) is $\dot{M}_* \sim 1 - 2 M_\odot \text{ yr}^{-1}$, while its gas mass is $M_g \sim 10^{10} M_\odot$. Thus, the time scale at which the Galaxy would deplete its gas while forming stars at the current rate is $\tau_{\text{dep}} \equiv M_g / \dot{M}_* \sim 5 - 10 \text{ Gyrs}$. The depletion time scales of a population of normal star-forming galaxies are comparable and span a range of $\sim 2 - 10 \text{ Gyrs}$ (Kennicutt 1989, 1998; Bigiel et al. 2008). The denser molecular phase of the interstellar medium (ISM) is depleted on a similarly long time scale of $\tau_{\text{dep,H}_2} \equiv M_{\text{H}_2} / \dot{M}_* \sim 1 - 3 \text{ Gyrs}$ (Kennicutt 1989, 1998; Wong & Blitz 2002; Bigiel et al. 2008; Leroy et al. 2008).

Compared to the time scales of any dynamical processes that are potentially relevant for star formation, the observed gas depletion times are very long indeed. For example, the orbital period of gas at the solar radius is $t_{\text{orb}} \sim 200 \text{ Myr}$, and the MW is thus depleting its gas on the time scale of $\sim 25 - 50$ such periods. On average, galaxies deplete their gas on the time scale of $\sim 10 - 20$ orbital periods (Kennicutt 1998; Wong & Blitz 2002; Leroy et al. 2008; Daddi et al. 2010).

The orbital period, t_{orb} , is probably the longest of the relevant dynamical time scales one can think of. For example, the

turbulent crossing time is usually $t_{\text{cross}} = h / \sigma \sim 10 - 30 \text{ Myr}$, where $\sigma \gtrsim 10 \text{ km s}^{-1}$ is the velocity dispersion of gas in galactic disks and $h \sim 100 - 300 \text{ pc}$ is the disk scale heights in the inner regions of galaxies. The free-fall time at the mean or midplane density, ρ_0 , of galaxies spans a similar range: $t_{\text{ff},0} \equiv \sqrt{3\pi / 32G\rho_0} \sim 10 - 50 \text{ Myr}$. The time scale of molecular clouds collisions is $\lesssim 20 \text{ Myr}$ (e.g., Tan 2000). A given gas mass encounters a spiral arm on a time scale of $t_{\text{arm}} \sim 2\pi / (m[\Omega(R) - \Omega_p])$, where $\Omega(R) = V_{\text{rot}} / R$ is the angular frequency of gas rotation, Ω_p is the pattern speed of spiral arms, and m is the number of spiral arms. This time scale is $t_{\text{arm}} \sim 50 - 200 \text{ Myr}$, if we assume $\Omega_p \sim 20 \text{ km s}^{-1} \text{ kpc}^{-1}$ (e.g., Bissantz et al. 2003), $m \sim 2 - 4$ (e.g., Davis et al. 2015) and $V_{\text{rot}} \sim 220 \text{ km s}^{-1}$ typically derived for MW-like galaxies. Numerical simulations of gaseous galactic disks show that star-forming molecular clouds may form on even shorter time scales of a few tens of Myrs (Dobbs et al. 2012, 2015).

In addition to being slow on global galactic scales, star formation is inefficient even in dense molecular star-forming regions, which convert only $\lesssim 1 - 10\%$ of gas into stars per local free-fall time (Zuckerman & Evans 1974; Zuckerman & Palmer 1974; Krumholz & Tan 2007; Krumholz et al. 2012; Evans et al. 2014; Lee et al. 2016; Heyer et al. 2016). Such low efficiency arises because only $\sim 0.1 - 10\%$ of the dense gas is self-gravitating and collapsing into stars (Froebrich & Rowles 2010).

However, the inefficiency of star-forming regions alone cannot explain long global depletion times. The local depletion time in observed star-forming regions is $t_* \sim 40 - 500 \text{ Myr}$ (e.g., Evans et al. 2009, 2014; Lada et al. 2010, 2012; Heiderman et al. 2010; Gutermuth et al. 2011; Schrubba et al. 2017). Thus, although the scatter is significant, typical values of t_* are considerably smaller than the global depletion time of molecular gas, $\tau_{\text{dep,H}_2} \sim 1 - 3 \text{ Gyr}$.

The large scatter in depletion times measured on small scales and the difference between local and global depletion time values indicate that only a fraction of molecular gas is ac-

¹ Department of Astronomy & Astrophysics, The University of Chicago, Chicago, IL 60637 USA

² Kavli Institute for Cosmological Physics, The University of Chicago, Chicago, IL 60637 USA

³ Enrico Fermi Institute, The University of Chicago, Chicago, IL 60637 USA

⁴ Fermilab Center for Particle Astrophysics, Fermi National Accelerator Laboratory, Batavia, IL 60510-0500 USA

* semenov@uchicago.edu

tively forming stars at any given moment. Indeed, the global depletion time can be expressed as:

$$\tau_{\text{dep}} \equiv \frac{M_{\text{g}}}{\dot{M}_{\text{sf}}} = \frac{\tau_{\star}}{f_{\text{sf}}}, \quad (1)$$

where M_{g} is the total gas mass of the galaxy, $\tau_{\star} \equiv M_{\text{sf}}/\dot{M}_{\star} = \langle 1/t_{\star} \rangle_{\text{sf}}^{-1}$ is the mass-weighted average over the depletion time distribution in star-forming regions, t_{\star} , and $f_{\text{sf}} \equiv M_{\text{sf}}/M_{\text{g}}$ is the gas mass fraction in actively star-forming regions. A similar expression can be written for the global depletion time of molecular gas, $\tau_{\text{dep,H}_2}$, via a corresponding star-forming fraction $f_{\text{sf,H}_2} \equiv M_{\text{sf}}/M_{\text{H}_2}$.

Thus, the depletion time measured on larger scales is longer than that in star-forming regions because as the scale increases, more of non-star-forming gas is incorporated in the gas mass estimate. Likewise, when depletion time is estimated on larger scales, the scatter in τ_{dep} decreases as we average over the distribution of local t_{\star} . This is indeed observed (Schruba et al. 2010, 2017), although some of the obtained variation may be due to observational effects (Feldmann et al. 2011; Kruijssen & Longmore 2014).

The small scatter in the global depletion time in observed galaxies is manifested in the Kennicutt-Schmidt relation (hereafter KSR) between the surface density of gas and star formation rate (Schmidt 1959; Kennicutt 1989, 1998, see also Sanduleak 1969; Madore et al. 1974). The relation is particularly tight and close to linear when only molecular hydrogen is used to estimate the surface density of gas (Wong & Blitz 2002; Bigiel et al. 2008). Thus, a comprehensive model for the global depletion time must explain not only its value, i.e., the normalization of the KSR, but also both the scatter and the shape of the KSR on different scales.

A number of useful global star formation frameworks and models have been developed over the last three decades (e.g., Wyse & Silk 1989; Silk 1997; Tan 2000; Elmegreen 2002; Krumholz & McKee 2005; Li et al. 2005; Saitoh et al. 2008; Krumholz et al. 2009b; Silk & Norman 2009; Ostriker et al. 2010; Ostriker & Shetty 2011; Renaud et al. 2012; Faucher-Giguère et al. 2013; Federrath 2013; Salim et al. 2015; Elmegreen 2015). Many of these models consider the physical processes shaping the form of the KSR, while treating its normalization as a flexible constant. Other models also consider the physical origin of the normalization and long depletion time scale.

One class of the latter models associates long depletion time with the fraction of gas in dense, self-gravitating regions of cold, supersonic molecular clouds with the log-normal gas density PDF (Elmegreen 2002; Krumholz & McKee 2005; Krumholz et al. 2012). Such models, however, assume that all of the molecular gas is in “virialized” star-forming molecular clouds and that the star formation efficiency in these clouds sets the global depletion time. This assumption, which has also been frequently adopted in galaxy simulations (e.g., Robertson & Kravtsov 2008; Gnedin et al. 2009; Kuhlen et al. 2012; Christensen et al. 2012), is at odds with a growing number of observations indicating that the depletion time of *star-forming* molecular gas is in general considerably shorter than the global depletion time of *all* molecular gas, $\tau_{\text{dep,H}_2}$, estimated on \gtrsim kpc scales. Moreover, models and simulations of star formation in supersonic turbulent clouds show that the local efficiency of star formation is primarily a strong function of the virial parameter of the region, not just its density, temperature, and molecular fraction (e.g., Krumholz & McKee

2005; Padoan et al. 2012, 2017), while the virial parameter can span a wide range of values (Dobbs et al. 2011; Semenov et al. 2016).

Some models derive the Kennicutt-Schmidt relation and its normalization by assuming that stellar feedback regulates ISM turbulence so as to maintain vertical and/or Toomre (1964) equilibrium within gaseous disks (Ostriker & Shetty 2011; Faucher-Giguère et al. 2013; Hayward & Hopkins 2017). However, it is not clear a priori why equilibrium can generically be expected in galaxies as a whole or in kiloparsec-scale patches and why star formation rate does not instead reach values, at which gas is driven out in a wind. Moreover, it is still debated whether the turbulence within galactic disks is mainly driven by stellar feedback or by gravitational instabilities (e.g., Krumholz & Burkhardt 2016).

Saitoh et al. (2008) argued that SFR is controlled by the rate at which gas is supplied from the general ISM to the star-forming state, which makes it insensitive to the local efficiency of star formation. However, these authors measured the time scale at which gas is supplied to the star-forming state to be ~ 100 Myr and did not explain how this time scale relates to the much longer observed depletion times of total gas, $\tau_{\text{dep}} \sim 2\text{--}10$ Gyrs.

In this paper, we aim to clarify the origin of the observed long gas depletion time scale in galaxies, taking into account both the inefficiency of star formation in star-forming clouds and the fact that not all of the molecular gas is actively forming stars. To this end, in Section 2 we present a simple conceptual framework that views the ISM as a highly dynamic medium in which gas evolves between non-star-forming and star-forming states. The key aspect of our framework is that it considers global gas depletion as a result of gas evolution which is driven by processes with associated characteristic time scales. This approach is conceptually similar to the framework of Kruijssen & Longmore (2014), developed to explain and interpret the scatter and possible biases in observational measurements of the Kennicutt-Schmidt relation on different scales.

We illustrate our framework using a realistic simulation of a galactic disk that reproduces the observed depletion time and the Kennicutt-Schmidt relation. We describe the simulation in Section 3. In Section 4 we demonstrate that the long global depletion time originates from the rapid cycling of ISM gas between non-star-forming and star-forming states on time scales $\sim 20\text{--}100$ Myr, in accord with the above estimates and the results of previous galactic disk simulations. On each such cycle, only a small fraction of gas mass is converted into stars and thus τ_{dep} is long because a large number of such cycles would be required to deplete all available gas. We analyze the processes driving the rapid gas evolution and also use simulations to shed light on the reason why the depletion time of molecular gas is nearly independent of the gas surface density. We discuss our results and summarize our conclusions in Sections 5 and 6.

2. A MODEL FOR GAS DEPLETION TIME

The interstellar gas in galaxies is a multiphase, dynamic medium spanning several orders of magnitude in density and temperature. To get a sense of the processes affecting the gas evolution in such a medium, we consider the evolution of individual gas parcels, massless tracers of gas flows in the ISM. One can think of a representative set of the ISM atoms as such tracers. At any given time, the local environment of such tracers can be estimated by averaging gas properties on some

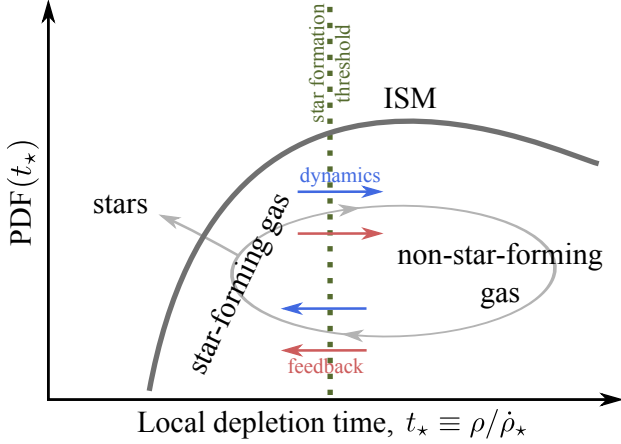


FIG. 1.— Schematic illustration of ISM gas evolution between non-star-forming and star-forming states. The thick gray line indicates the mass-weighted PDF of local gas depletion times, $t_* \equiv \rho / \dot{\rho}_*$, where ρ and $\dot{\rho}_*$ are the local densities of gas and SFR. The vertical dotted line corresponds to the threshold depletion time, $t_{*,\max}$, separating star-forming and non-star-forming gas. The gray loop illustrates cycling of a gas parcel between these states under the influence of dynamical and feedback processes. Averaging over the entire ensemble of gas parcels results in the total mass fluxes directed into and out of the star-forming state (indicated with straight blue and red arrows).

scale l around the position of each tracer. The gas around tracers will expand and contract under the influence of dynamical processes, such as turbulence driven by gravitational instabilities and stellar feedback. Therefore, during evolution over a sufficiently long time scale, the conditions around each gas parcel can evolve between the states of long and short depletion time, t_* , once or over many transition cycles. Such cycling of gas parcels is schematically shown in Figure 1.

The probability density per unit time for a parcel to be converted into a star is given by $1/t_*$ and one can define the depletion time for a single parcel as the time required for the integrated probability to reach unity. In what follows, for conceptual simplicity we will adopt a sharp threshold, $t_{*,\max}$, separating non-star-forming, $t_* > t_{*,\max}$, and actively star-forming, $t_* < t_{*,\max}$, gas states. For a given distribution of t_* , this threshold can be chosen in a way that regions with $t_* < t_{*,\max}$ include most of the total star formation.

The duration of a single cycle between the successive stages when the parcel's environment is in the star-forming state equals to the sum of the times spent in the non-star-forming, t_{nsf} , and star-forming, t_{sf} , stages. If we denote the average depletion time of the parcel during the star-forming stage as τ_* , the parcel will have a probability of t_{sf}/τ_* to be converted into a star during the entire cycle. In other words, $N_c = \tau_*/t_{\text{sf}}$ such cycles would be needed for the parcel to be incorporated into a star. Its depletion time can thus be written as:

$$t_{\text{dep}} = N_c(t_{\text{nsf}} + t_{\text{sf}}) = N_c t_{\text{nsf}} + \tau_* = \left(\frac{t_{\text{nsf}}}{t_{\text{sf}}} + 1 \right) \tau_*. \quad (2)$$

Hence, the depletion time of a gas parcel is always longer than τ_* and can be long because star formation during t_{sf} is inherently inefficient, i.e., τ_* is long, and/or because only a small fraction of the evolution cycle is spent in the star-forming state, i.e., $t_{\text{nsf}}/t_{\text{sf}}$ is large.

A group of parcels in a patch of the ISM has a distribution of τ_* , t_{sf} , t_{nsf} and the collective depletion time of the group is the average $\tau_{\text{dep}} = \langle 1/t_{\text{dep}} \rangle^{-1}$ over these distributions. It is clear that if the depletion times of individual parcels are long,

τ_{dep} will also be long.

In practice, τ_{dep} of an ISM patch is estimated from the instantaneous mass of gas, M_g , and young stars formed over a time interval Δt in this patch, $M_*(\Delta t)$, such that the average star formation rate is $\langle \dot{M}_* \rangle_{\Delta t} = M_*(\Delta t)/\Delta t$ and the depletion time is defined as $\tau_{\text{dep}} \equiv M_g / \langle \dot{M}_* \rangle_{\Delta t}$. This estimate of τ_{dep} can be related to the dynamics of individual gas parcels within the patch by noting that due to mass conservation, the instantaneous total mass of gas parcels in the star-forming state, M_{sf} , evolves as $\dot{M}_{\text{sf}} = F_{\text{sf}} - \dot{M}_*$, where F_{sf} is the net instantaneous flux of gas parcels through the star formation threshold and \dot{M}_* is the instantaneous SFR of all parcels. After averaging this expression over the time interval Δt , we get:

$$\tau_{\text{dep}} \equiv \frac{M_g}{\langle \dot{M}_* \rangle_{\Delta t}} = \frac{M_g}{\langle F_{\text{sf}} \rangle_{\Delta t} - \langle \dot{M}_{\text{sf}} \rangle_{\Delta t}}. \quad (3)$$

For brevity, in the following derivation we omit explicit averaging, $\langle \dots \rangle_{\Delta t}$, but assume all fluxes and rates to be averaged over Δt .

In general, the average net flux of gas through the star formation threshold can be decomposed into positive and negative contributions illustrated with the straight arrows in Figure 1:

$$F_{\text{sf}} = F_+ - F_-. \quad (4)$$

The positive flux F_+ is controlled by a combination of global dynamical processes, e.g., gravitational instabilities, turbulence, cooling, etc., with a significant contribution from stellar feedback. The latter comes in the form of turbulence stirred by interactions of supernova-driven bubbles and by fountain outflows of gas from star-forming regions. The negative flux $F_- = F_{-\text{fb}} + F_{-\text{d}}$ results from the destruction of star-forming regions both by feedback from young stars formed inside the regions, $F_{-\text{fb}}$, as well as by shearing due to large-scale turbulence or differential rotation, expansion of gas behind galactic spiral arms and other dynamical processes not directly related to star formation inside the regions, $F_{-\text{d}}$. All fluxes can be parametrized with the characteristic time scales, i.e., τ_+ , $\tau_{-\text{fb}}$ and $\tau_{-\text{d}}$, on which gas is supplied to and removed from the star-forming state by the corresponding processes:

$$F_+ \equiv \frac{M_{\text{nsf}}}{\tau_+} = M_g \frac{1 - f_{\text{sf}}}{\tau_+}, \quad (5)$$

$$F_- \equiv \frac{M_{\text{sf}}}{\tau_-} = F_{-\text{fb}} + F_{-\text{d}} = M_g f_{\text{sf}} \left(\frac{1}{\tau_{-\text{fb}}} + \frac{1}{\tau_{-\text{d}}} \right), \quad (6)$$

where $f_{\text{sf}} \equiv M_{\text{sf}}/M_g$ is the star-forming mass fraction.

To make the relation between star formation and stellar feedback explicit, we can also parametrize $F_{-\text{fb}}$ in a way similar to the parametrization of the mass outflow rate of feedback-driven galactic winds:

$$F_{-\text{fb}} \equiv \xi \dot{M}_* = M_g f_{\text{sf}} \frac{\xi}{\tau_*}, \quad (7)$$

where ξ is the *mass loading factor* and we used the definition of the average depletion time of *star-forming gas*, $\tau_* \equiv M_{\text{sf}}/\dot{M}_*$. In the context of Equation (6) the mass loading factor can also be interpreted as a relative rate of gas removal by feedback compared to the rate of star formation, i.e., $\xi \equiv \tau_*/\tau_{-\text{fb}}$.

Imbalance between the net gas flux into the star-forming state, F_{sf} , and the average SFR may result in the evolution

of the star-forming mass, which we also parametrize with the characteristic time scale, $\tau_{e,sf}$:

$$|\dot{M}_{sf}| \equiv \frac{M_{sf}}{\tau_{e,sf}}. \quad (8)$$

The final expression for the global depletion time can be readily derived by substituting Equations (4-8) and $f_{sf} = \tau_*/\tau_{dep}$ into Equation (3):

$$\tau_{dep} = \left(1 + \xi + \frac{\tau_*}{\tau_{-,d}} \pm \frac{\tau_*}{\tau_{e,sf}} \right) \tau_+ + \tau_*, \quad (9)$$

where the sign in front of $\tau_*/\tau_{e,sf}$ reflects the sign of \dot{M}_{sf} .

If we compare the terms in this equation with those in Equation (2) for the depletion time of a single gas parcel, $t_{dep} = N_c t_{nsf} + \tau_*$, their physical meaning becomes clear. The time scale τ_+ is analogous to the time t_{nsf} that a gas parcel spends in the non-star-forming state, while the expression in parenthesis is analogous to $N_c = \tau_*/t_{sf}$, i.e., the average number of evolution cycles it would take for a single parcel to deplete its gas. Indeed, Equation (5) gives $M_{nsf} = F_+ \tau_+$, which means that τ_+ is the time over which all of the non-star-forming gas will reach the star-forming state. Thus, τ_+ is analogous to the average t_{nsf} time scale for a collection of parcels. Likewise, the average rate at which gas mass in the star-forming state is decreasing due to star formation, dispersal and the overall evolution of the gas PDF during Δt is given by $M_{sf}/\tau_* + M_{sf}/\tau_- \pm M_{sf}/\tau_{e,sf}$, and the associated time scale $(1/\tau_* + 1/\tau_- \pm 1/\tau_{e,sf})^{-1}$ corresponds to the average time gas spends in this state. Thus, on average, gas will have to reach the star-forming state

$$N_c = \tau_* \left(\frac{1}{\tau_*} + \frac{1}{\tau_-} \pm \frac{1}{\tau_{e,sf}} \right) = 1 + \xi + \frac{\tau_*}{\tau_{-,d}} \pm \frac{\tau_*}{\tau_{e,sf}}, \quad (10)$$

times, where we used Equation (6) and the definition of the mass loading factor, $\xi \equiv \tau_*/\tau_{-,fb}$.

Equation (9) is the key expression of our framework. It states that *the global depletion time is the sum of the total time that gas spends in the non-star-forming state over N_c cycles and the total time over which star-forming regions convert this gas into stars, τ_* .*

This equation elucidates how long τ_{dep} values can be reconciled with the relatively short local depletion times, τ_* , and even shorter dynamical time scales, τ_+ , discussed in the Introduction. The global depletion time is longer than the depletion time in star-forming regions, τ_* , due to the significant fraction of time that gas spends in the non-star-forming state. The global depletion time is longer than the time scale associated with dynamical processes supplying star-forming gas, τ_+ , because gas must evolve through the non-star-forming state N_c times, and N_c is large due to either efficient feedback, i.e., large ξ , or fast dynamical processes destroying star-forming regions, i.e., short $\tau_{-,d}$ (see Equation 10).

When feedback dominates removal of gas from the star-forming state, the number of cycles becomes $N_c \sim \tau_*/\tau_{-,fb}$. This clarifies how feedback can self-regulate star formation, i.e., how τ_{dep} can become insensitive to τ_* . Indeed, the time scale $\tau_{-,fb}$ is proportional to the rate of energy and momentum injection by feedback, which, in turn, is set by the local rate of star formation, i.e., τ_* . Hence, $\tau_{-,fb} \propto \tau_*$, which renders N_c insensitive to τ_* . Thus, when $N_c \tau_+ \gg \tau_*$, the depletion time, $\tau_{dep} \approx N_c \tau_+$, will be insensitive to τ_* .

In a non-equilibrium state, in which $\dot{M}_{sf} > 0$ (< 0) during Δt , the term $\pm \tau_*/\tau_{e,sf}$ in Equation (9) accounts for the correction of the average rates estimated using the star-forming gas fraction, f_{sf} , defined for the instantaneous masses M_{sf} and M_g . Such a correction is required because when $\dot{M}_{sf} > 0$ (< 0) the actual average fraction of Δt that gas spends in the star-forming state is smaller (higher) than f_{sf} and therefore more (fewer) transition cycles are required for depletion.

In a steady state, on the other hand, the gas distribution is stationary and the star formation rate is in equilibrium with the gas fluxes into and out of the star-forming state: $\dot{M}_{sf} = F_{sf} - \dot{M}_* \approx 0$. In this case, $\tau_{e,sf} \rightarrow \infty$ and the term $\tau_*/\tau_{e,sf}$ can be neglected in Equation (9). In such a steady state, $\tau_{dep} = M_g/F_{sf}$ (see Equation 3), and depletion time is determined by the *net* rate of gas inflow into the star-forming state, F_{sf} . When F_{sf} is small, the depletion time is long. Galaxies as a whole reach the steady state with $\dot{M}_{sf} \approx 0$ on the shortest of the time scales that control the global depletion time in Equation (9). Thus, globally, such an assumption is justified. However, individual ISM patches may deviate from the steady state, and the $\tau_*/\tau_{e,sf}$ term will be one of the sources of the scatter in depletion time.

In the remainder of the paper, we illustrate the framework described above using the results of an isolated galaxy simulation. Although the simulation adopts specific choices for many parameters including resolution and prescriptions for star formation and feedback, the overall features and implications of our model do not depend on these specific choices. Our framework generically allows one to relate the depletion time on a large scale, e.g., the scale of entire galaxy, to the star formation and feedback model that operates on a smaller scale, e.g., resolution scale of a simulation, where the distribution of local depletion times, t_* , is defined.

3. SIMULATION

To illustrate the framework outlined above and elucidate the physical processes that give rise to long global depletion times, we use a simulation of an isolated $\sim L_*$ -sized galaxy. We carried out the simulation with the Adaptive Mesh Refinement N -body and gas dynamics code ART (Kravtsov 1999; Kravtsov et al. 2002; Rudd et al. 2008; Gnedin & Kravtsov 2011) and followed the evolution of an isolated gaseous disk in a live potential of a dark matter halo, stellar bulge, and stellar disk that are modeled with collisionless particles.

We adopt initial conditions that were used in the AGORA code comparison project (Kim et al. 2016) and also in the studies of Agertz et al. (2013) and Semenov et al. (2016). Specifically, the isolated disk is initialized inside a dark matter halo with $v_{c,200} = 150 \text{ km s}^{-1}$ and the initial concentration of $c = 10$. The initial disk of old stars has an exponential density profile with a radial scale length of $r_d \approx 3.4 \text{ kpc}$ and a vertical scale height of $h_d = 0.1 r_d$ with the total mass of $M_{*,d} \approx 3.4 \times 10^{10} M_\odot$. The stellar bulge has an initial mass of $M_{*,b} \approx 4.3 \times 10^9 M_\odot$ that is distributed with a Hernquist density profile with $a = 0.1 r_d$ (Hernquist 1990). The initial exponential gaseous disk has the same r_d and h_d as the stellar disk; its total mass is $M_g \approx 8.6 \times 10^9 M_\odot$, which corresponds to the disk gas fraction of $f_g \equiv M_g/(M_{*,d} + M_g) = 20\%$.

Gas evolution is governed by modified hydrodynamical equations that include terms related to cooling and heating, dynamical effects of subgrid turbulence, gas consumption by star formation, and injection of mass, momentum and energy by feedback from young stars.

Cooling in the optically thin limit is implemented following the model of Gnedin & Hollon (2012). We assume a fixed metallicity of $Z = Z_\odot$ and constant background heating by interstellar radiation in the Lyman-Werner band with the photodissociation rate of 10^{-10} s^{-1} (Stecher & Williams 1967). To model temperatures in dense self-shielded gas we assume that extinction is proportional to the local column density of atomic gas, which we approximate as $nL_{J,40}$, where n is the gas number density in a cell and $L_{J,40}$ is the local Jeans length with an applied temperature ceiling of 40 K (model “L1a” in Safraneck-Shrader et al. 2017).

In our simulation we adopt the unresolved turbulence model of Schmidt et al. (2014) that dynamically follows the kinetic energy of gas motions on subgrid scales, K , as a separate hydrodynamical field akin to thermal energy. Subgrid turbulence is generated by random velocities on the resolution scale; it exerts pressure and viscous forces on resolved gas motions and decays on the local cell-crossing time scale, as motivated by simulations of both subsonic and supersonic turbulence (e.g., Mac Low et al. 1998). For details about the model implementation in ART we refer to Semenov et al. (2016).

We adaptively resolve cells where the total gas mass exceeds $\sim 8300 M_\odot$ and reach a maximum resolution of $\Delta = 40 \text{ pc}$. Such a Δ is sufficient to resolve ISM structure down to densities of $n \sim 100 - 1000 \text{ cm}^{-3}$ and therefore we do resolve the dynamical processes that are sometimes claimed to limit star-forming gas supply from the general ISM with average density of $n \sim 1 \text{ cm}^{-3}$. At the highest resolution level we do not apply an artificial pressure floor in cold gas. Thus, the densities of star-forming regions are limited only by the effects of stellar feedback and the effective pressure due to thermal and both subgrid and resolved turbulent motions.

As a star formation prescription we adopt the local rate $\dot{\rho}_* = \rho/t_*$, where ρ is the gas density in a cell, and the local depletion time, t_* , is related to the free-fall time, $t_{\text{ff}} \equiv \sqrt{3\pi/32G\rho}$, with the efficiency per free-fall time, $t_* = t_{\text{ff}}/\epsilon_{\text{ff}}$. Numerical and analytical models of star formation in turbulent GMCs generally predict a strong increase of ϵ_{ff} with increasing relative importance of gravity that facilitates star formation, in comparison to turbulence that provides support against gravity (for a review, see Padoan et al. 2014). For example, Padoan et al. (2012) found that the star formation efficiency of a turbulent cloud increases exponentially with decreasing virial parameter, $\epsilon_{\text{ff}} \approx \exp(-\sqrt{\alpha_{\text{vir}}/0.53})$, where α_{vir} is defined for a box with a side Δ as for a uniform sphere of radius $R = \Delta/2$:

$$\alpha_{\text{vir}} \equiv \frac{5\sigma_{\text{ID}}^2 R}{GM} \approx 9.35 \frac{(\sigma_{\text{tot}}/10 \text{ km s}^{-1})^2}{(n/100 \text{ cm}^{-3})(\Delta/40 \text{ pc})^2}. \quad (11)$$

In our simulations, to apply the Padoan et al. (2012) fit in thermally supported gas, in the definition of α_{vir} we consider contributions of both the sound speed, c_s , and the explicitly modeled subgrid turbulent velocities, $\sigma_t \equiv \sqrt{2K/\rho}$:

$$\sigma_{\text{tot}} = \sqrt{\sigma_t^2 + c_s^2}. \quad (12)$$

Also, even though we are able to model ϵ_{ff} following the Padoan et al. (2012) formula (see, e.g., Semenov et al. 2016; Li et al. 2017), in the simulation used here, we approximate the continuous exponential dependence of ϵ_{ff} on α_{vir} assuming a constant $\epsilon_{\text{ff}} = 1\%$ for $\alpha_{\text{vir}} < \alpha_{\text{vir,sf}} = 10$, and $\epsilon_{\text{ff}} = 0$ elsewhere. This simulation was carried out as part of a simulation suite in which ϵ_{ff} value was varied systematically to explore its effect

on star formation in galaxies. Using a constant ϵ_{ff} and a sharp $\alpha_{\text{vir,sf}}$ threshold makes interpretation of simulation results easier and we will present the results of this simulation suite in a forthcoming study. We explicitly checked that the global depletion times and the Kennicutt-Schmidt relations are similar in runs where ϵ_{ff} follows the Padoan et al. (2012) fit and where we approximate this fit with a threshold. A qualitatively similar star formation prescription but with a different choice of parameters was studied by Hopkins et al. (2013).

We stress that the scenario of gas depletion described in Section 2 remains valid for any choice of star formation prescription, although in Section 5.2 we argue that such prescription should be chosen carefully, as it is important for prediction of realistic ISM properties. We note that our adopted threshold value, $\alpha_{\text{vir,sf}} = 10$, is consistent with the observed distribution of α_{vir} in molecular clouds, which is peaked at $\alpha_{\text{vir}} \sim 10$ for the clouds with sizes comparable to our resolution of $\Delta = 40 \text{ pc}$ (Miville-Deschênes et al. 2017). The adopted value of $\epsilon_{\text{ff}} = 1\%$ is consistent with the average values deduced for observed actively star-forming clouds.

In our feedback prescription, we inject momentum and energy from the type II SNe at a uniform rate between 3 and 43 Myr after the formation of a stellar particle. The total number of SNe exploded over this time interval is computed assuming the Chabrier (2003) IMF. The thermal energy and radial momentum injected by each supernova are calibrated against simulations of a SN remnant evolution in a non-uniform medium (Martizzi et al. 2015), taking into account ambient gas density, and with an additional boost of radial momentum by a fiducial factor of 5. We adopt such a boosting factor to compensate for the numerical loss of injected momentum and to account for the actual physical uncertainties of the radial momentum estimates (e.g., Gentry et al. 2017). In addition to SNe type II feedback, during evolution, stellar particles return a fraction of their mass following the prescription of Leitner & Kravtsov (2011).

Figure 2 shows the spatial distribution of gas number density, temperature, and subgrid turbulent velocity in our simulated galaxy at $t = 500 \text{ Myr}$. The figure highlights the multiphase, dynamic structure of the ISM. Comparison with a simulation with no feedback, that we will present in a companion paper, shows that the structure of the ISM is significantly affected by stellar feedback. Its effect is manifested not only in the ubiquitous regions of hot, turbulent gas but also in the overall flocculent nature of the spiral pattern.

In our analysis, we estimate the molecular gas density in each cell using the KMT model (Krumholz et al. 2008, 2009a; McKee & Krumholz 2010): $\rho_{\text{H}_2} = \max[0, (1 - 0.75s)/(1 + 0.25s)]\rho$, where at solar metallicity $s \approx 1.8/\tau_c$ and $\tau_c = 320(\rho\Delta/\text{g cm}^{-2})$. This model predicts a rapid increase of the molecular fraction at densities $n > 10 \text{ cm}^{-3}$ indicated by the black contour in Figure 2. The resulting total mass fraction of molecular gas in our simulation is $f_{\text{H}_2} \equiv M_{\text{H}_2}/M_g \sim 20\%$.

Subgrid turbulent velocities, σ_t , range from $\lesssim 3 \text{ km s}^{-1}$ in the diffuse ISM between spiral arms to $\sim 30 - 300 \text{ km s}^{-1}$ in hot SNe bubbles. In this simulation supernovae do not explicitly inject turbulent energy and high σ_t in hot bubbles are generated by the subgrid turbulence model. In the cold, dense gas turbulent velocities are supersonic and also vary significantly, $\sigma_t \sim 5 - 15 \text{ km s}^{-1}$. Strong subgrid turbulence in cold gas results in high values of α_{vir} and according to our star formation criterion, $\alpha_{\text{vir}} < \alpha_{\text{vir,sf}} = 10$, only $\sim 40\%$ of all molecular gas mass is star-forming at any given moment. Such star-forming

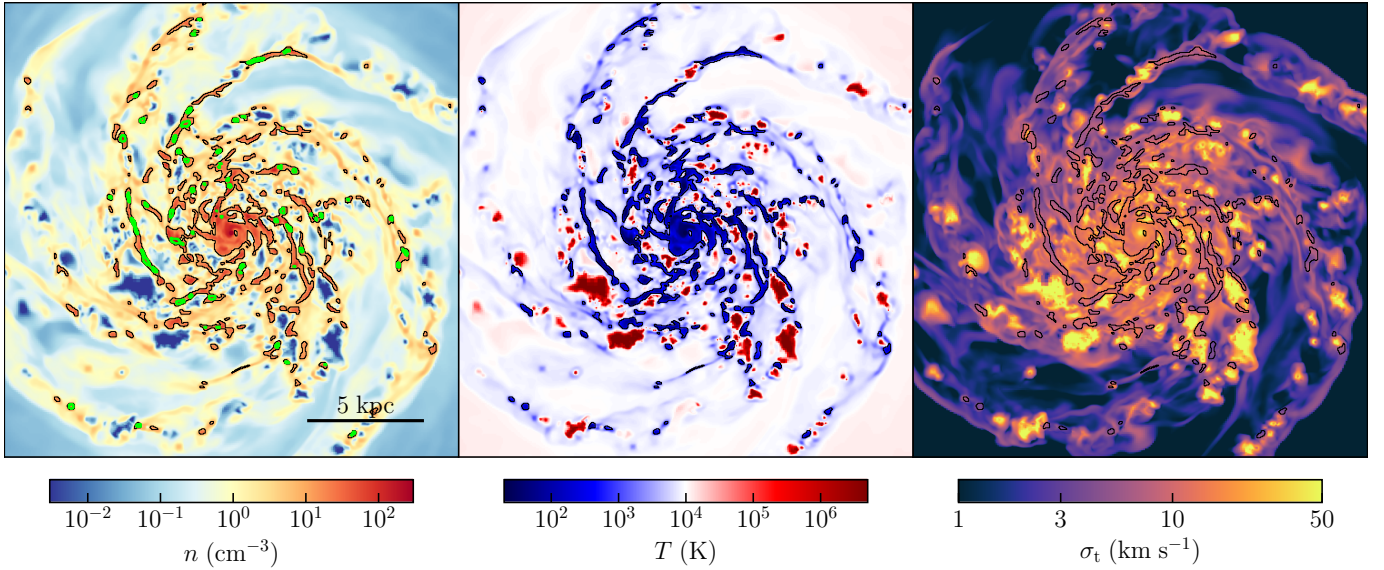


FIG. 2.— Midplane slices of gas number density, n , temperature, T , and subgrid turbulent velocity, $\sigma_t = \sqrt{2K/\rho}$, after 500 Myr of evolution. To make comparison easier, the black contours in all panels correspond to $n = 10 \text{ cm}^{-3}$, above which molecular mass fraction rapidly increases at solar metallicity. Green contours in the left panel indicate gas that satisfies our star formation criterion: $\alpha_{\text{vir}} < \alpha_{\text{vir,sf}} = 10$.

regions are shown in the left panel with the solid green contours.

The total SFR of our model galaxy is $\dot{M}_* \sim 1 - 2 \text{ M}_\odot \text{ yr}^{-1}$, which translates to global depletion times of total and molecular gas of $\tau_{\text{dep}} \sim 4 - 8 \text{ Gyr}$ and $\tau_{\text{dep,H}_2} \sim 1 - 2 \text{ Gyr}$. The values of depletion times and molecular fraction are in the ballpark of the typical values observed in nearby spiral galaxies (e.g., Wong & Blitz 2002; Bigiel et al. 2008).

Figure 3 compares the Kennicutt-Schmidt relation between the surface densities of SFR and $\text{H I} + \text{H}_2$ and H_2 gas in our simulation to the observed relations in the Milky Way and nearby spiral galaxies. Our results are in a good agreement both in normalization (i.e., the depletion time value) and slope. Note, in particular, that the linear relation between $\dot{\Sigma}_*$ and Σ_{H_2} emerges from the non-linear star formation prescription adopted in our simulation: $\dot{\rho}_* \propto \rho^{1.5}$. In Section 4.4, we consider the origin of the linear relation and show that it results from the particular behavior of the gas density distribution shaped by stellar feedback.

For a consistent comparison with the observed KSR for $\text{H I} + \text{H}_2$ gas, in our simulation we defined neutral hydrogen to be all non-molecular gas denser than $n_{\text{H,SSH}}$, given by Equation (13) in Rahmati et al. (2013). This threshold corresponds to the gas self-shielded from the far ultraviolet (FUV) background with the adopted photoionization rate $\Gamma = 10^{-10} \text{ s}^{-1}$. We also excluded all neutral hydrogen that is colder than 1000 K assuming that it constitutes optically thick cold neutral medium (CNM) not included into the observed measurements of Σ_{HI} . Our temperature threshold is somewhat higher than the CNM temperature estimated in real galaxies ($\lesssim 300 \text{ K}$, e.g., Wolfire et al. 2003) because in our simulation we do not resolve the transition between warm and cold neutral gas phases, which results in intermediate gas temperatures on the resolution scale. The particular value of the temperature threshold was chosen to select $\sim 40\%$ of the neutral hydrogen mass, which is close to the CNM mass fractions estimated in the Milky Way and nearby galaxies (e.g., Heiles & Troland 2003; Braun 2012; Pineda et al. 2013; Sofue 2017).

In the analyses presented below, we consider the processes in the ISM during the time interval between 400 and 600 Myr, which is short enough to neglect the effect of global gas consumption on the ISM dynamics and long enough to accumulate sufficient statistics of rare events and make the considered distributions representative and well-sampled.

To study the detailed dynamics of individual gas parcels we use gas tracer particles that are passively advected with the local flow velocity interpolated to the positions of the particles with the cloud-in-cell scheme. We populate the disk with 10^5 tracer particles uniformly initialized within $R < 8 \text{ kpc}$ after 300 Myr of disk evolution when the transients related to the initial off-equilibrium state had dissipated away. After initialization, we wait for 100 Myr to let tracers equilibrate with the gas density distribution. At that point, the distributions of tracer densities in radial annuli resemble the gas density PDF in computational cells and distribution of tracer properties thus can be considered to be a good approximation of the mass-weighted PDF of gas properties.

We average the distribution of tracers to construct statistics, such as their PDF and fluxes in the $n - \sigma_{\text{tot}}$ phase diagram, between 400 and 600 Myr with 1 Myr step. We checked that at every moment between 400 and 600 Myr phase distributions of gas and tracer particles resemble their averaged versions, which means that the galaxy remains in approximate equilibrium over the considered period of time.

We focus on the evolution of gas in the phase plane of density, n , and total velocity dispersion, σ_{tot} , because the position of a gas parcel in this plane determines its internal consumption time, t_* , according to our star formation prescription. To quantify gas motions in the $n - \sigma_{\text{tot}}$ plane we measure the derivatives $d \log n / dt$ and $d \log \sigma_{\text{tot}} / dt$ probed by each tracer every 1 Myr. To estimate the average local flow rates of gas, we accumulate fluxes corresponding to these derivatives and normalize them by the local density of tracers in the $n - \sigma_{\text{tot}}$ plane.

To characterize actual fluxes that supply and remove star-forming gas, in addition to the total flux of tracers, we separately track fluxes of tracers with decreasing or increasing

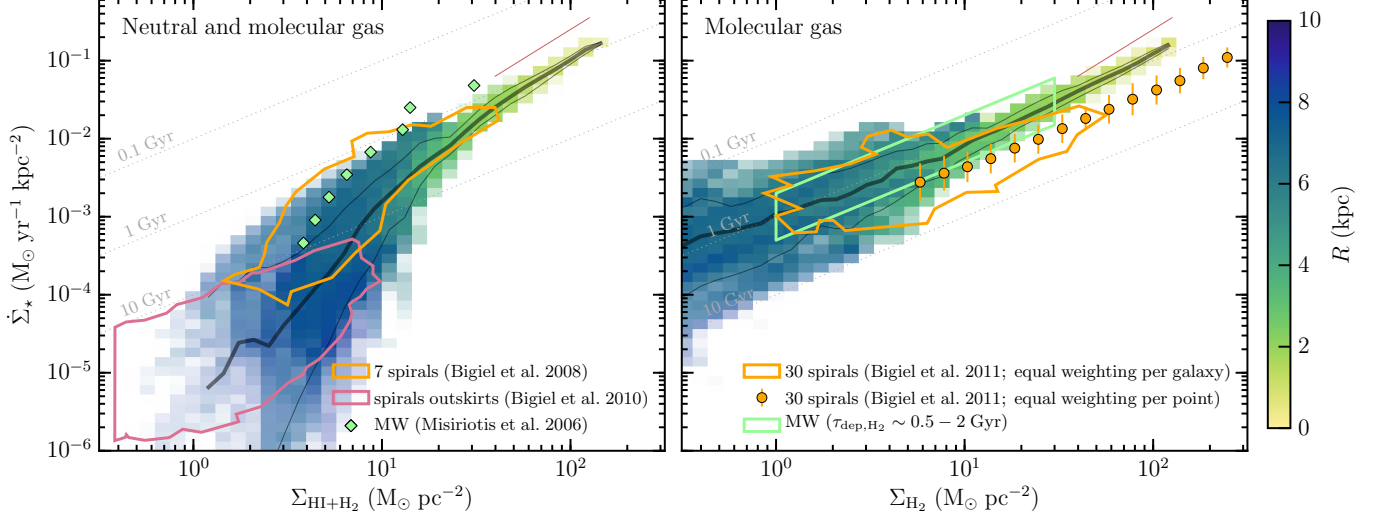


FIG. 3.— The relation between the surface density of SFR and total (left panel) and molecular gas (right panel) in our simulation and in observations. To match the typical spatial scales on which this relation is usually measured, we smooth 2D maps of $\dot{\Sigma}_*$ and $\Sigma_{\text{HI}+\text{H}_2}$ obtained at 500 Myr with a Gaussian filter with a width of 1 kpc and plot the median, 16th, and 84th percentiles of the resulting pixel distribution (thick and thin gray lines). The distributions are colored according to the average galactic radius, R , of pixels in a given bin. To match the averaging time scales of star formation indicators, we measure the surface density of stars that are younger than 30 Myr and define $\dot{\Sigma}_*$ as $\Sigma_*(< 30 \text{ Myr}) / 30 \text{ Myr}$. The thin red line at high Σ indicates the slope adopted in our star formation prescription, $\dot{\rho}_* \propto \rho^{1.5}$. Thin dotted lines correspond to the constant depletion times of 0.1, 1 and 10 Gyr (from top to bottom). We compare our results to the observed relations in nearby spiral galaxies (Bigiel et al. 2008, 2010, 2011) and in the Milky Way (Misiriotis et al. 2006). The green contour in the right panel shows the range of $\tau_{\text{dep,H}_2} \sim 0.5 - 2 \text{ Gyr}$ estimated using the radial profiles of $\dot{\Sigma}_*$ and Σ_{H_2} for the Milky Way from Figure 7 in Kennicutt & Evans (2012).

α_{vir} . We quantify the magnitudes of these fluxes with the characteristic evolution time scale, on which α_{vir} changes by an order of magnitude at a given rate:

$$\tau_{\alpha, \gtrless 0} \equiv \left\langle \left| \frac{d \log_{10} \alpha_{\text{vir}}}{dt} \right| \right\rangle_{\gtrless 0}^{-1}, \quad (13)$$

where we average the derivative of $\log_{10} \alpha_{\text{vir}}$ taking into account only tracers with decreasing (increasing) α_{vir} to compute $\tau_{\alpha, < 0}$ ($\tau_{\alpha, > 0}$).

4. RESULTS

4.1. The origin of long global depletion time

As we discussed at the end of Section 2, in steady state, when $\langle \dot{M}_{\text{sf}} \rangle_{\Delta t} \approx 0$ on the time scale Δt over which SFR is estimated, long global depletion time, $\tau_{\text{dep}} \equiv M_{\text{g}} / \dot{M}_{\text{sf}} = M_{\text{g}} / F_{\text{sf}}$, originates from a small *net* flux of gas into the star-forming state, F_{sf} . In principle, F_{sf} could be small if the rate at which gas evolves towards the star-forming state were set by a slow “bottleneck” process. However, as Figure 4 shows, in simulations with efficient feedback gas rapidly transitions between the star-forming and non-star-forming states, and a small F_{sf} results from a near cancellation of large opposite fluxes into and out of the star-forming state.

In this figure we plot the distribution of gas tracer particles within the disk in the plane of gas number density, n , and $\sigma_{\text{tot}} = \sqrt{\sigma_t^2 + c_s^2}$, that can be viewed as an effective temperature including both thermal and turbulent gas motions on subgrid scales. The gas distribution spans a wide range of densities, σ_{tot} , and temperatures and has two distinct peaks. The peak at low densities, $n \sim 1 \text{ cm}^{-3}$, corresponds to diffuse, warm, subsonic ($\sigma_t \lesssim c_s$) gas at temperature $T \sim 10^4 \text{ K}$. The gas in the second peak at $n > 10 \text{ cm}^{-3}$, on the other hand, is cold ($T \lesssim 100 \text{ K}$) and supersonic ($\sigma_t > c_s$).

According to our star formation prescription, the star-forming gas has $\alpha_{\text{vir}} < \alpha_{\text{vir, sf}} = 10$. Such gas in the diagram resides below the diagonal thick dotted line. The net mass flux of gas in the $n - \sigma_{\text{tot}}$ plane is visualized with the arrows in the upper panel of Figure 4, where the length of the arrows is equal to the distance tracers would traverse in 5 Myr for a given flux. The figure shows that arrows are rather small throughout most of the phase space occupied by tracers and it is particularly small near the thick dotted line. This means that the *net* evolution of gas in $n - \sigma_{\text{tot}}$ plane is slow and the net flux through the star formation threshold, F_{sf} , is small. This small net flux results in the long global depletion time scales exhibited by our simulated galaxy, $\tau_{\text{dep}} \sim 5 \text{ Gyr}$ and $\tau_{\text{dep,H}_2} \sim 1 \text{ Gyr}$ (see Section 3 and Figure 3).

However, the middle and bottom panels of Figure 4 show that the small net F_{sf} results from the near cancellation of two opposite fluxes. These panels show the fluxes of only those tracers which α_{vir} is decreasing, F_+ , or increasing, F_- , and these fluxes are significantly stronger than the net flux in the upper panel. A typical tracer evolves towards and away from the star-forming state on the time scale of order $\tau_{\alpha, \gtrless 0} \sim 5 - 30 \text{ Myr}$, consistent with the estimates of the time scales of relevant processes in Section 1. Thus, the rate of gas supply from the diffuse, warm ISM to the star-forming state cannot be the factor limiting the global star formation rate, as envisioned by Saitoh et al. (2008). Instead, gas generally evolves from the diffuse to star-forming state on the time scale of tens of Myr, much shorter than the global depletion time. The latter is long because gas rapidly leaves the star-forming state at the rate that nearly cancels the rate at which gas is reaching this state. In the next section we consider the processes that drive the fast gas evolution in more detail.

4.2. Dynamical processes shaping ISM

The average gas flow patterns shown with arrows in Figure 4 result from the statistical averaging of the complicated

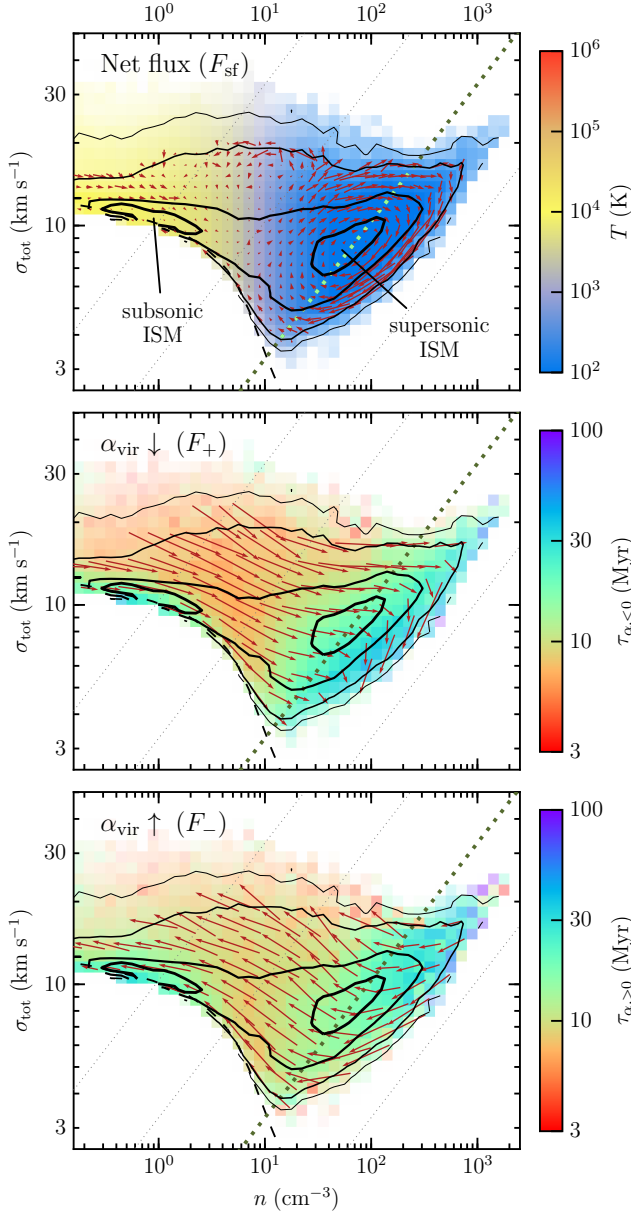


FIG. 4.— The distribution of gas tracer particles in the plane of gas number density, n , and total velocity dispersion, $\sigma_{\text{tot}} = \sqrt{\sigma_t^2 + c_s^2}$, averaged between 400 and 600 Myr. The black contours in all panels indicate the averaged PDF of tracers and correspond to 20, 68, 95 and 99% of all tracers. The diagonal dotted lines indicate constant values of α_{vir} from left to right: 1000, 100, 10, 1, with $\alpha_{\text{vir}} = \alpha_{\text{vir,sf}} = 10$ shown with the thick green dotted line. The dashed line along the lower envelope of the PDF at $n < 10 \text{ cm}^{-3}$ indicates the median sound speed, c_s , in each density bin. Colors in the top panel show average gas temperature in each bin, while arrows indicate average total fluxes of gas tracers measured as described at the end of Section 3. Arrows in the middle and bottom panels correspond to the fluxes of gas tracers with decreasing and increasing α_{vir} respectively. Colors in these panels show the distribution of the characteristic evolution time scales, $\tau_{\alpha,\geq 0}$, defined by Equation (13). The normalizations of arrows are the same in all three panels and correspond to the distances that tracers would traverse at a given rate over 5 Myr.

trajectories of individual tracer particles. Particular shapes of such trajectories vary depending on local conditions and specific physical processes that govern gas evolution.

In our simulation, gas evolution between diffuse, warm, subsonic and dense, cold, supersonic ISM phases is governed by large-scale disk instabilities and turbulent flows gener-

ated by them. The evolution of gas in the dense phase is determined predominantly by stellar feedback that disperses star-forming regions, drives large-scale ISM turbulence and launches fountain-like outflows.

In the following subsections we consider these processes using three representative tracer trajectories integrated over 200 Myr and shown in Figure 5. We chose these particular tracers because their evolution over the considered period of time is governed predominantly by the same process over several consequential cycles of compression and expansion.

4.2.1. Compression and expansion due to spiral arms

The blue line in the upper left panel of Figure 5 shows an example of the α_{vir} evolution followed by a tracer that swings between the subsonic and supersonic phases during cycles of compression and expansion as it enters and exits spiral arms. The trajectory of this tracer in the $n - \sigma_{\text{tot}}$ plane is shown with the same color in the right panel.

Due to strong compression gas entering a spiral arm rapidly cools down and loses thermal support that initially dominates in subsonic ISM. At the same time, initially low subgrid turbulent velocities of subsonic ISM, $\sigma_t \lesssim 3 \text{ km s}^{-1}$, rapidly grow due to compressional heating (see the detailed discussion in Section 3.1 of Semenov et al. 2016 and also Robertson & Goldreich 2012). At $n \sim 10 \text{ cm}^{-3}$, when subgrid turbulent velocities become comparable to the thermal speed, gas detaches from the lower envelope of the distribution shown in Figure 4 and enters the supersonic ISM phase. Similarly, when gas leaves a spiral arm, it expands, and subgrid turbulent velocities decrease. Eventually, under the influence of expansion and interstellar FUV heating, gas returns to the subsonic ISM phase with $n \sim 1 \text{ cm}^{-3}$ and $T \sim 10^4 \text{ K}$.

The actual transition of gas between subsonic and supersonic phases is fast as it is controlled by strong compression rate in spiral arms and short cooling times at $n > 1 \text{ cm}^{-3}$. Hence, the rate at which diffuse gas is promoted into the dense phase is mostly determined by the time that gas waits between subsequent passages of spiral arms:

$$\tau_{\text{arm}} \sim \frac{2\pi R}{mV_{\text{gas}}} \sim 80 \text{ Myr} \frac{(R/8 \text{ kpc})}{(m/6)(V_{\text{gas}}/100 \text{ km s}^{-1})}, \quad (14)$$

where $V_{\text{gas}} \equiv v_{\text{gas}} - v_{\text{pat}}$ is the speed of gas relative to the spiral waves pattern, and we set $m = 6$ as our simulated galaxy develops six spiral arms.

Typical time that gas spends inside a spiral arm before expansion contributes to the dynamical rate of gas removal from the star-forming state, τ_{d} . This time scale depends on the spiral arm width, gas velocity and the angle at which gas flows inside the arm. Depending on local conditions, this time scale can be as long as few tens of Myrs.

In Figure 6 we plot distributions of n and σ_{tot} separately for tracers residing at different galactic radii and therefore experiencing different ISM conditions. The distribution in the outer disk (upper panel) is shaped predominantly by the compression and expansion due to spiral arms. Specifically, most of the gas mass in the outer disk resides in the diffuse subsonic phase and forms a peak at $n \sim 1 \text{ cm}^{-3}$ and $T \sim 10^4 \text{ K}$. The tail extending along the lower envelope of the distribution towards the dense supersonic phase corresponds to the gas currently being compressed in spiral arms. As the figure also shows, compression of diffuse gas in spiral arms is only relevant at large radii, whereas closer to the disk center less gas

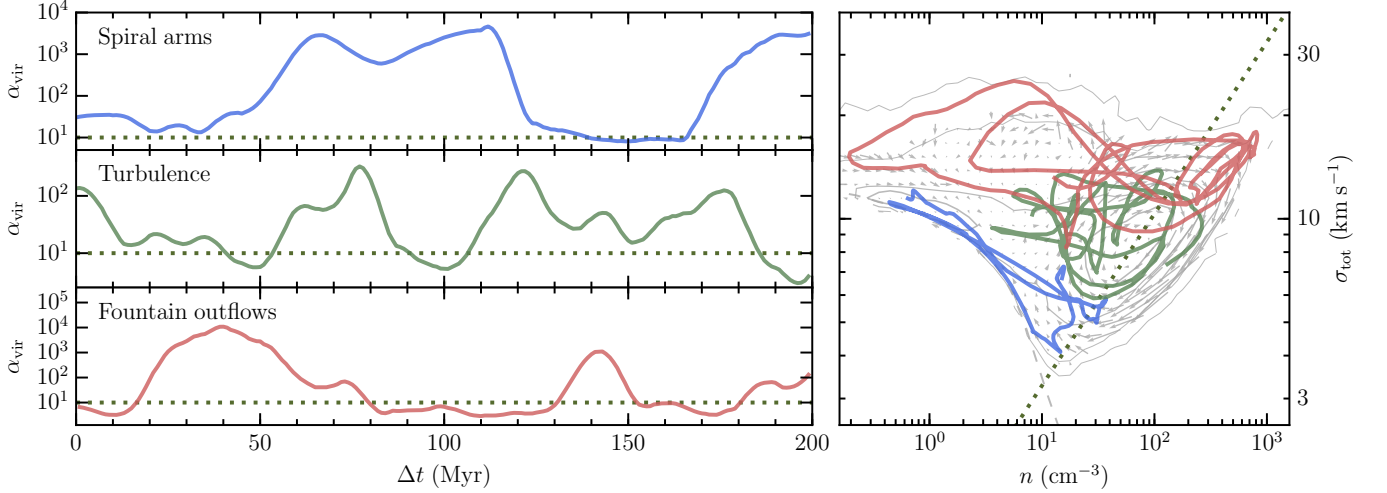


FIG. 5.— Trajectories of three representative tracers followed for 200 Myr. The left set of panels shows the evolution of α_{vir} for each of the three tracers. The right panel shows the trajectories in the $n - \sigma_{\text{tot}}$ plane with the corresponding colors. The gray contours and arrows indicate average tracers PDF and their net fluxes as in the upper panel of Figure 4. The thick dotted lines in all panels correspond to the adopted star formation threshold, $\alpha_{\text{vir}} = \alpha_{\text{vir,sf}} = 10$. For presentation purposes, small fluctuations of actual tracer trajectories on time scales $\lesssim 5$ Myr were smoothed using Savitzky-Golay filter.

remains in the diffuse phase and this process becomes much less important.

4.2.2. SNe-induced shocks and ISM turbulence

We find that the evolution of dense, supersonic gas in the $n - \sigma_{\text{tot}}$ plane is dominated by the turbulence that is driven by stellar feedback. Injection of momentum by SNe in a star-forming region results in a rapid expansion of gas until the region is eventually dispersed. Shocks associated with expanding bubbles compress gas in the disk plane, which may induce new episodes of star formation and subsequent SNe explosions. The turbulence resulting from overlapping and interacting bubbles makes gas parcel to oscillate in fast cycles, as illustrated by the green trajectory in Figure 5.

The characteristic time scale between subsequent compressions of ISM gas by such expanding SNe shocks corresponds to:

$$\tau_{\text{shell}} \sim \frac{L}{v_{\text{shell}}} \sim 50 \text{ Myr} \frac{(L/1 \text{ kpc})}{(v_{\text{shell}}/20 \text{ km s}^{-1})}, \quad (15)$$

where L is a typical separation between bubbles (see, e.g., temperature map in the middle panel of Figure 2) and v_{shell} is a typical velocity of shells on scale L .

Compression and expansion of gas in the turbulent ISM is accompanied by increase and decrease of turbulent velocity dispersion. As a result, averaging of such large-scale turbulent motions over many tracers results in a prominent clockwise whirl-like pattern of arrows around the peak of the PDF in the cold (blue) part of the diagram (see Figures 4 and 6). Closer to the peak center the net flux magnitude decreases due to the averaging between fast motions of many tracers at the different stages of their turbulent compression-expansion cycles.

As Figure 6 shows, such whirlwind pattern is most prominent at $R \leq 6$ kpc. Thus, the feedback-driven turbulence and associated compression and expansion of gas are dominant processes at these radii in the cold, supersonic gas. ISM at these radii has a complex structure (see Figure 2) reflecting the chaotic turbulent nature of the gas.

4.2.3. Feedback-driven fountain outflows

Supernova feedback also affects some of the gas by accelerating it in the direction perpendicular to the disk plane. Such gas expands in fountain-like outflows, but eventually cycles back to the ISM under the influence of the disk potential. Interactions of such outflows with the halo gas adjacent to the disk result in an increase of small-scale turbulent velocities that quickly dissipate when gas falls back onto the disk.

An example of a tracer trajectory during expansion and subsequent recycling of a fountain outflow is shown with the red line in Figure 5. This particular tracer was ejected and recycled twice, at ~ 20 – 80 and ~ 130 – 150 Myr. In each event, after its star-forming region was dispersed by feedback, this tracer acquires a moderate vertical velocity of $v_z \sim 50 \text{ km s}^{-1}$ and elevates as high as ~ 400 pc above the disk plane, i.e., a few scale heights, before falling back onto the disk. In the highest elevation point the gas in these outflows expands only to the densities comparable to those of the diffuse subsonic ISM phase, $n \sim 0.2$ – 2 cm^{-3} and its virial parameter reaches the values of $\alpha_{\text{vir}} \sim 10^3$ – 10^4 due to the strong turbulence generated by the interaction of expanding outflow with the surrounding gas. Outflows launched by feedback from regions of more vigorous star formation reach even lower n and higher α_{vir} .

The time scale of the fountain cycle can be estimated as a dynamical time in the gravitational field of a massive infinite sheet of constant surface density Σ_{tot} , corresponding to the local total surface density of the disk:

$$\tau_{\text{grav}} \sim \frac{v_z}{\pi G \Sigma_{\text{tot}}} \sim 20 \text{ Myr} \frac{(v_z/50 \text{ km s}^{-1})}{(\Sigma_{\text{tot}}/200 \text{ M}_{\odot} \text{ pc}^{-2})}, \quad (16)$$

where v_z is the initial vertical velocity of gas in the outflow and $\Sigma_{\text{tot}} = \Sigma_{\star} + \Sigma_{\text{g}} \sim 200 \text{ M}_{\odot} \text{ pc}^{-2}$ is the typical total surface density of gas and stars in our simulated galaxies.

The averaging of trajectories between many gas parcels constituting fountain-like outflows results in a tail of the distribution directed from the star-forming state towards the lower densities and higher σ_{tot} . The total flux of tracers forms a prominent counter-clockwise vortex inside this tail clearly seen in Figures 4 and 6.

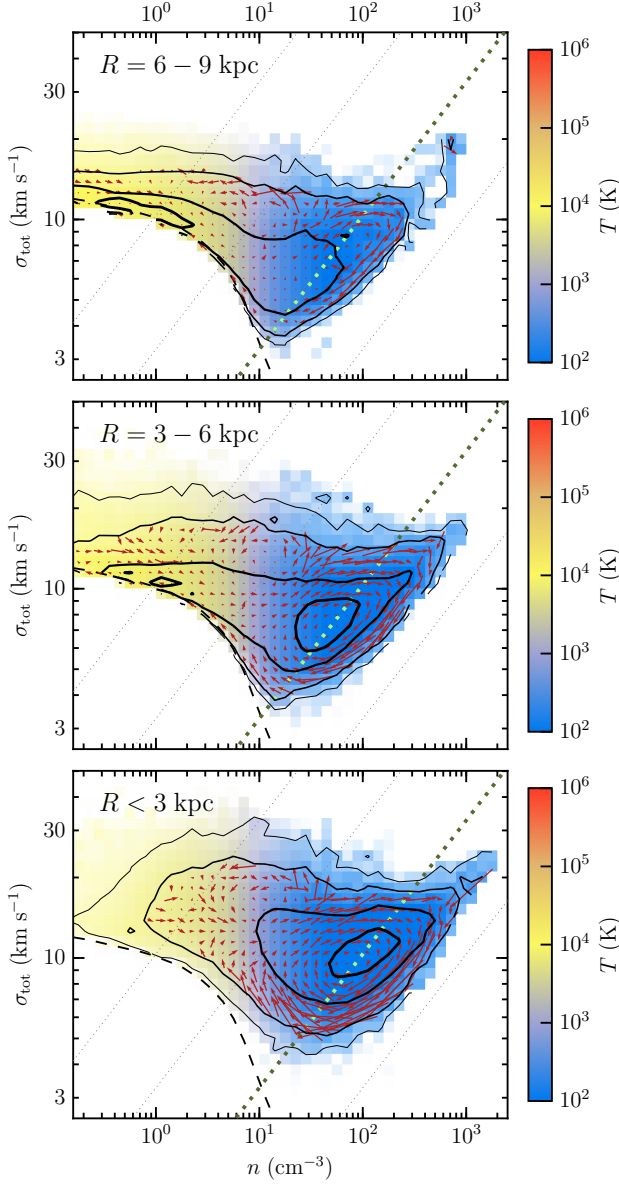


FIG. 6.— Distributions and average fluxes of tracers residing at different galactic radii, R (shown in the upper left corner of each panel). Notation follows that of the upper panel of Figure 4. Comparison with the right panel of Figure 5 hints that the distribution of tracers on the disk outskirts (upper panel) is predominantly shaped by gas compression and expansion due to spiral arms, while close to the disk center (bottom panel) the distribution is shaped by feedback-driven turbulence and outflows. Whirl-like patterns of velocities in the cold, supersonic phase indicate that distribution of dense gas at all radii is affected by star formation feedback (see text for details).

Figure 6 shows that at all radii within the disk some fraction of gas evolves in the manner discussed above, which indicates the existence of fountain-like outflows. At larger radii, where the SFR is slower, the outflows are less prominent but still visible as a net flux of tracers directed towards lower densities along the upper envelope of the distribution shown in the upper panel. Gas in such outflows at large radii usually returns to the diffuse, warm, subsonic ISM in-between spiral arms. Closer to the center, outflows are ubiquitous, and after falling back, their gas directly rejoins tumultuous large-scale turbulent motions of dense, supersonic gas.

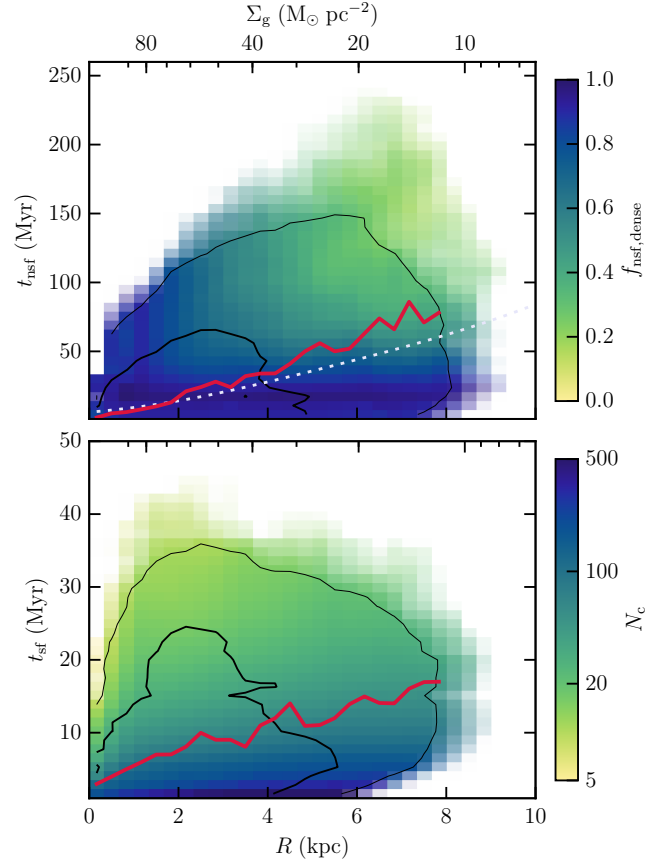


FIG. 7.— The distribution of time that tracers spend in non-star-forming (t_{nsf} , top panel) and star-forming (t_{sf} , bottom panel) states between successive crossings of the star formation threshold. Distributions of t_{nsf} and t_{sf} are shown as a function of galactic radius, R . Top axis in each panel also indicates the average surface density of gas at a given radius, $\Sigma_g \propto \exp(-R/r_d)$, where r_d is the initial scale radius of the disk. Contours indicate 68 and 95% of trajectories. The thick red lines show the median time scales at every radius. The light dotted line in the upper panel corresponds to the free-fall time at the average midplane density at a given radius. Colors in the top panel show the average fraction of time spent in the dense phase with $n > 10 \text{ cm}^{-3}$: $f_{\text{nsf,dense}} \equiv t_{\text{nsf,dense}}/t_{\text{nsf}}$. Colors in the bottom panel show the average number of passages through the star-forming state required for complete depletion, N_c (Equation 17). To increase the statistics for long cycles, we follow tracers between 400 and 1000 Myr of the disk evolution. For presentation purposes, we smooth the resulting distributions preserving their main features.

4.3. Duration and number of evolution cycles

Typical tracer trajectories considered in the previous section explicitly confirm that during the evolution gas parcels perform many fast cycles and rapidly explore a significant portion of the PDF extent frequently switching between non-star-forming and star-forming states. As we discussed in Section 2, the distribution of times that gas parcels spend on each cycle in these states, t_{nsf} and t_{sf} , determines the global depletion time of the galaxy.

In Figure 7 we plot the distribution of t_{nsf} and t_{sf} directly measured from the trajectories of all tracers as the times between consequential crossings of the star formation threshold. Results in the previous section indicate that the mix of the processes governing gas evolution may change with the galactic radius, R , and surface density, Σ_g . Thus, to explore possible trends, we plot the distributions of time scales as a function of R and Σ_g .

The distribution of t_{nsf} shown in the upper panel indicates that the majority of tracers spends less than 100 Myr in the

non-star-forming stage of evolution during each cycle. At higher average surface densities closer to the disk center this time is even shorter, $t_{\text{nsf}} \lesssim 50$ Myr, with a very low median value (thick red line).

Color in the upper panel shows the average fraction of time that gas tracers spend in the dense phase, $n > 10 \text{ cm}^{-3}$, over the non-star-forming stage of evolution. Blue color at small radii implies that gas preferentially stays in the dense, molecular phase even when it does not form stars. This is also evident from the lower panel of Figure 6, which shows that only a small fraction of gas expands to $n < 10 \text{ cm}^{-3}$ and it does so as a part of fountain outflows.

At larger radii, the relatively slow rate of star-forming gas replenishment via compression in spiral arms becomes important and the median t_{nsf} increases to ~ 80 Myr. Gas governed by this process spends significant time in the diffuse subsonic ISM, and such tracer trajectories occupy the areas of the longest t_{nsf} at $R > 4$ kpc (green color). However, as indicated by the blue color, at such radii many tracers still perform short cycles with $t_{\text{nsf}} < 50$ Myr without leaving the dense phase.

The increase of the t_{nsf} median value is consistent with the scaling proportional to the free-fall time at the mean or mid-plane density at a given radius, $t_{\text{ff},0} \propto \rho_0^{-1/2} = (\Sigma_g/2h_d)^{-1/2}$, shown by the dotted line (see also Saitoh et al. 2008). Such scaling is sometimes adopted in analytical models of galactic star formation to define the time scale on which star-forming regions are created (e.g., Krumholz et al. 2012; Elmegreen 2015). As we discussed above, t_{nsf} in our simulations is set by both stellar feedback that drives turbulence and dynamical processes within the ISM. The scaling of the median t_{nsf} with density indicates that gravity and associated time scale plays at least some role in setting the time that gas spends in the non-star-forming state. For example, the fall of the gas driven out in a fountain outflow back to the disk will occur on the time scale of order $\sim t_{\text{ff},0}$.

The bottom panel of Figure 7 shows the distribution of times spent by tracers in the star-forming state on each cycle. This time scale is close to the typical “lifetime” of star-forming regions and is quite short: $t_{\text{sf}} \lesssim 20$ Myr or 2–4 free-fall times at the typical densities of star-forming regions. The fact that t_{sf} is on average significantly shorter than t_{nsf} is consistent with the small mass fraction of star-forming gas.

As we discussed in Section 2, the average time that a gas parcel spends in the star-forming state on a single cycle determines the total number of such cycles required for complete depletion as $N_c = \tau_*/t_{\text{sf}}$. For every tracer on each passage through the star-forming stage we estimate this number as the inverse fraction of mass depleted over the passage:

$$N_c^{-1} = \int \frac{dt}{t_*} = \int \epsilon_{\text{ff}} \frac{dt}{t_{\text{ff}}}, \quad (17)$$

where the integral is accumulated for each tracer particle while it is in the star-forming state between subsequent crossings of the star formation threshold. The resulting distribution of N_c is shown with colors in the bottom panel.

In agreement with our model, typical $N_c \sim 50$ and the lifetimes of gas in the star-forming state, $t_{\text{sf}} \sim 10$ –20 Myr, are consistent with the range of the star-forming gas depletion times, $\tau_* \sim N_c t_{\text{sf}} \sim 300$ –500 Myr, obtained in our simulation (see the next subsection). In addition, assuming $t_{\text{nsf}} \sim 50$ –100 Myr, Equation (2) for the typical depletion time of a gas parcel gives a value of ~ 2 –5 Gyr, which is consistent

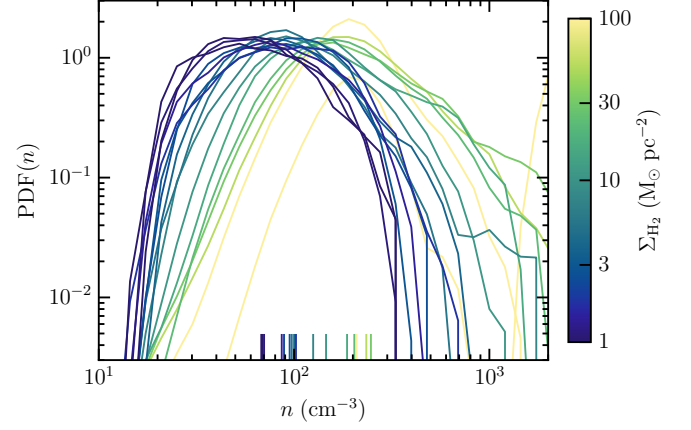


FIG. 8.— Mass-weighted number density PDFs of star-forming gas in 500 pc wide radial annuli. The line colors show the average surface density of molecular gas in a given radial annulus, Σ_{H_2} . The vertical colored ticks indicate $\langle \sqrt{n} \rangle_{\text{sf}}$, i.e., the average density that determines the star-forming gas depletion time in a given annulus: $\tau_* \propto \langle \sqrt{n} \rangle_{\text{sf}}^{-1}$. To improve sampling, we accumulate the shown star-forming gas distributions between 400 and 600 Myr of disk evolution.

with the actual global depletion time obtained in our simulation (see Section 3).

4.4. Emergence of linear $\dot{\Sigma}_* - \Sigma_{\text{H}_2}$ relation

One of the most intriguing results of our simulation is the emergence of the linear $\dot{\Sigma}_* - \Sigma_{\text{H}_2}$ relation consistent with observations (see the right panel of Figure 3), even though on small scales the star formation rate is assumed to scale non-linearly with the gas density: $\dot{\rho}_* = \epsilon_{\text{ff}} \rho / t_{\text{ff}} \propto \rho^{1.5}$. This result provides a counter-example to the arguments that in simulations the slope of the Kennicutt-Schmidt relation on large and small scales should be the same (Schaye & Dalla Vecchia 2008; Gnedin et al. 2014).

The observed linearity of the molecular KSR is often explained by the “counting argument,” which posits that all molecular gas is in star-forming clouds of approximately the same depletion time. In this case, the surface density of SFR will vary linearly with the surface density of molecular gas, as long as the geometric covering fraction of star-forming clouds is less than unity.

However, if not all of the molecular gas is star-forming, as is the case in our simulations and is likely the case in observed galaxies, the explanation for the linearity must be more nuanced. Analogously to Equation (1), the depletion time of molecular hydrogen is given by

$$\tau_{\text{dep,H}_2} \equiv \frac{\Sigma_{\text{H}_2}}{\dot{\Sigma}_*} = \frac{\tau_*}{f_{\text{sf,H}_2}}, \quad (18)$$

where $f_{\text{sf,H}_2} \equiv \Sigma_{\text{sf}}/\Sigma_{\text{H}_2}$. The linearity of the molecular KSR, or, equivalently, independence of $\tau_{\text{dep,H}_2}$ of Σ_{H_2} , must therefore arise from a lack of dependence of τ_* and $f_{\text{sf,H}_2}$ on Σ_{H_2} or a cancellation of any such dependence in their ratio.

The depletion time of star-forming gas is given by the average over the inverse local depletion time distribution in star-forming regions, $\tau_* \equiv \Sigma_{\text{sf}}/\dot{\Sigma}_* = \langle 1/t_* \rangle_{\text{sf}}^{-1}$. Thus, if the distribution of t_* is independent of Σ_{H_2} , so is τ_* , regardless of the actual shape of the distribution. In our simulation $t_* = t_{\text{ff}}/\epsilon_{\text{ff}}$, where $\epsilon_{\text{ff}} = \text{const}$, and thus the distribution of $t_* \propto n^{-1/2}$ is set by the density distribution of star-forming gas.

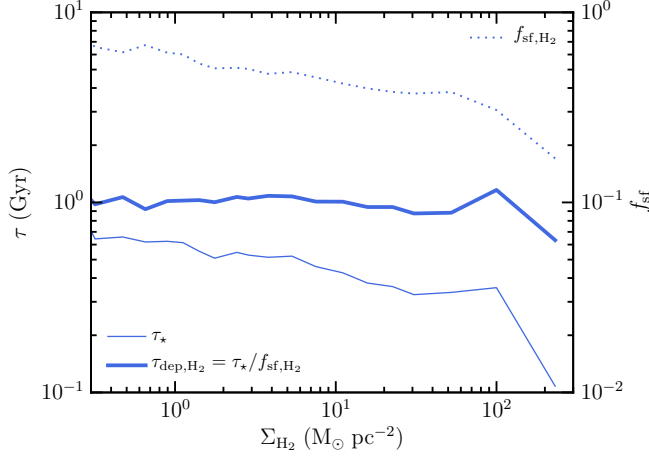


FIG. 9.— The dependence of molecular gas depletion time, $\tau_{\text{dep,H}_2}$ (solid line, left axis), star-forming gas depletion time, τ_* (thin line, left axis), and the star-forming mass fraction of molecular gas, $f_{\text{sf,H}_2}$ (dotted line, right axis), on the average surface density of molecular gas, Σ_{H_2} , in radial annuli with widths of 500 pc. The trends of τ_* and $f_{\text{sf,H}_2}$ with Σ_{H_2} cancel each other in the expression for the molecular gas depletion time, $\tau_{\text{dep}} = \tau_*/f_{\text{sf,H}_2}$, which results in a linear KSR for molecular gas.

The PDFs of star-forming gas density in radial annuli with widths of 500 pc are shown in Figure 8. The figure shows that Σ_{H_2} spans two orders of magnitude, while the average star-forming gas density and the shape of the PDF do vary, but the variation is quite mild. Thus, τ_* depends on Σ_{H_2} , but weakly, as shown by the thin line in Figure 9.

This dependence is weak for two reasons. First, the average density of star-forming gas in all of the ISM environments in our simulation is limited by the stellar feedback (at high densities) and FUV background (at $n < 20 \text{ cm}^{-3}$) to a nearly constant range of $n \sim 10\text{--}10^3 \text{ cm}^{-3}$, comparable to the typical densities of observed star-forming regions. Second, as in the counting argument, Σ_{H_2} varies mostly due to the variation of the geometric covering fraction of molecular gas, not due to the change of its density.

As the dotted line in Figure 9 shows, the star-forming mass fraction, $f_{\text{sf,H}_2}$, also varies weakly with Σ_{H_2} , with the dependence on Σ_{H_2} similar to that of τ_* . In Equation (18) the weak trends of τ_* and $f_{\text{sf,H}_2}$ with Σ_{H_2} cancel resulting in a constant $\tau_{\text{dep,H}_2}$, which explains the origin of the linear $\dot{\Sigma}_* - \Sigma_{\text{H}_2}$ relation.

Such almost exact cancellation of $f_{\text{sf,H}_2}$ and τ_* trends implies that $f_{\text{sf,H}_2} \propto \tau_*$. Some co-variance of $f_{\text{sf,H}_2}$ with τ_* is expected because τ_* controls the rate of feedback energy and momentum injection. As a result, longer τ_* results in less turbulence, i.e., smaller α_{vir} and larger $f_{\text{sf,H}_2}$. This qualitative explanation, however, will need to be investigated and tested more thoroughly with simulations and will be a subject of our future study.

5. DISCUSSION

The short, $\sim 10\text{--}100$ Myr, time scales of the physical processes driving the evolution of gas in the ISM (see the upper panel of Figure 7) indicate that the ISM is vigorously “boiling” when considered on the global depletion time scale. During this vigorous evolution, gas cycles between non-star-forming and star-forming stages and spends only $t_{\text{sf}} \sim 5\text{--}15$ Myr in the star-forming stage on each cycle (see the lower panel of Figure 7), which is consistent with the short

lifetimes derived for observed GMCs (e.g., Kawamura et al. 2009; Murray 2011; Schruha et al. 2017).

Observational estimates of the integral star-formation efficiency during a star-forming stage, defined for a given star-forming region containing a gas mass of m_g and a mass of formed young stars of m_* as $\epsilon_{\text{int}} \equiv m_*/(m_g + m_*)$, give $\epsilon_{\text{int}} \sim 1\text{--}20\%$ (e.g., Evans et al. 2009; Lada et al. 2010). This fraction is even smaller in less efficient clouds (e.g., Rebolledo et al. 2015; Lee et al. 2016; Vutisalchavakul et al. 2016). A similar range of ϵ_{int} is also obtained in simulations of star cluster formation (Gavagnin et al. 2017) and cosmological simulations of a Milky Way-sized galaxy that resolve the growth of globular clusters and self-consistently capture its termination by stellar feedback (Li et al. 2017).

Such values of ϵ_{int} imply that gas parcels must undergo $N_c \sim \epsilon_{\text{int}}^{-1} \sim 5\text{--}100$ cycles transitioning from the non-star-forming to star-forming state before they convert their gas into stars. This number of cycles is also consistent with the typical depletion times of star-forming gas, $\tau_* \equiv \langle 1/t_* \rangle_{\text{sf}}^{-1}$, and lifetimes, t_{sf} , derived for observed star-forming regions, $N_c = \tau_*/t_{\text{sf}}$. Specifically, depletion times of gas in observed star-forming regions are estimated to be $t_* \sim 50\text{--}500$ Myr (e.g., Evans et al. 2009, 2014; Lada et al. 2010, 2012; Heiderman et al. 2010; Gutermuth et al. 2011; Schruha et al. 2017); for $t_{\text{sf}} \sim 5\text{--}15$ Myr quoted above, these t_* give $N_c \sim (50\text{--}500)/(5\text{--}15) \sim 3\text{--}100$. Such N_c are in the ballpark of the N_c range that we estimate for the gas in our simulations (see the lower panel of Figure 7), although we note that the number of cycles in our simulation can be somewhat overestimated due to the artificially sharp threshold in the definition of star-forming gas.

Note that the specific values of t_{nsf} , t_{sf} and N_c depend on the scale, l , on which the small-scale distribution of t_* is defined. Clearly, if we consider the evolution of gas parcels on the scale of protostellar cores, ~ 0.01 pc, the star-forming stage of evolution will correspond to the formation of one or a handful of stars, which will consume most of the gas in a single event. The gas parcels on this scale will spend a long time in the non-star-forming stage and will consume their gas in one or a few cycles, $N_c = 1 + \xi$, where ξ corresponds to the ratio of the protostellar core mass returned back to the ISM to the mass of the formed star.

Note also that the overall physical explanation for long gas depletion times presented in Sections 2 and 4 does not rely on the assumption of dynamical equilibrium. When a gas parcel undergoes some inherently non-equilibrium process, such as compression in a spiral arm, the parcel’s depletion time will still be given by $t_{\text{dep}} = (\tau_*/t_{\text{sf}})(t_{\text{nsf}} + t_{\text{sf}}) = \tau_*(t_{\text{nsf}}/t_{\text{sf}} + 1)$, and therefore t_{dep} will be long if $t_{\text{nsf}} \gg t_{\text{sf}}$ and/or τ_* is long. Absence of a long-term equilibrium requirement is an essential difference of our framework from the models for the Kennicutt-Schmidt relation that rely on the assumption of self-regulation to the vertical or Toomre (1964) equilibrium state (e.g., Ostriker & Shetty 2011; Faucher-Giguère et al. 2013).

In fact, our model explicitly accounts for the deviations from an equilibrium state, in which $\dot{M}_{\text{sf}} \approx 0$. Such deviations, along with the fluctuations of other quantities that enter Equation (9), can be important sources of the depletion time scatter. These deviations can be substantial for individual ISM patches, which generally will not be in equilibrium, even if a galaxy as a whole is. Additional scatter can arise due to observational tracers sampling different stages of gas evolution incompletely (Kruijssen & Longmore 2014).

We note, however, that unlike the models of Ostriker & Shetty (2011) and Faucher-Giguère et al. (2013), our conceptual framework cannot quantitatively predict the depletion time by itself. It only elucidates how the depletion time is related to the time scales of processes driving gas evolution. The variables through which this relation is parametrized can either be calibrated in simulations, as is done in this study, or be derived in analytical models. Nevertheless, as we discuss in the following subsections, our framework is very useful for interpreting and explaining a number of puzzling facts about star formation in both observed and simulated galaxies.

5.1. Implications for observations

Rapid cycling of gas between non-star-forming and star-forming states explains the large discrepancy between long global depletion times of $\gtrsim 1$ Gyr and short, ~ 10 – 100 Myr, time scales associated with the dynamical processes in the ISM. Only a small fraction of gas is converted into stars during each cycle and therefore gas would have to go through a large number of cycles to be depleted.

Our model also naturally explains the difference between observed local depletion times of (mostly molecular) gas in star-forming regions, $t_\star \sim 50$ – 500 Myr, and global depletion times of both total gas, $\tau_{\text{dep}} \sim 2$ – 10 Gyr, and molecular gas, $\tau_{\text{dep,H}_2} \sim 1$ – 3 Gyr. The global depletion times, τ_{dep} and $\tau_{\text{dep,H}_2}$, are longer than the average gas depletion time in star-forming regions, τ_\star , due to the significant fraction of time that gas spends in the non-star-forming state (see Equation 2). This implies that only a fraction of total and molecular gas is forming stars at any given moment. For example, the observed values of t_\star and $\tau_{\text{dep,H}_2}$ indicate that only $f_{\text{sf,H}_2} \equiv M_{\text{sf}}/M_{\text{H}_2} = \tau_\star/\tau_{\text{dep,H}_2} \sim 5$ – 50% of molecular gas is forming stars. The range of $f_{\text{sf,H}_2}$ in our simulation is consistent with this estimate (see the dotted line in Figure 9), with the non-star-forming molecular gas state corresponding to strongly turbulent cold gas.

As pointed out by Kruijssen & Longmore (2014), a model considering different evolutionary stages and corresponding chemical phases of the ISM gas can be used to interpret dependence of the depletion time and its scatter on the averaging scale (see, e.g., Schruba et al. 2017). This dependence in observed galaxies can be also used as a stringent test of the star formation and feedback implementation in galaxy formation models.

Our model for gas depletion time provides a natural framework for predicting and interpreting trends with galaxy properties and redshift. For instance, we show that the duration of cycles decrease with increasing surface density as $t_{\text{nsf}} \propto \Sigma_g^{-0.5}$, which is accompanied by a milder but nevertheless non-negligible decrease in τ_\star (see Section 4.4 and the thin line in Figure 9). This means that the observed decrease in global depletion times in high-redshift and starburst galaxies (e.g., Kennicutt 1998; Bouché et al. 2007; Genzel et al. 2010; Tacconi et al. 2017) can be explained by shorter dynamical time scales, t_{nsf} , and star-forming gas depletion times, τ_\star , associated with high-density environments. In addition, the non-equilibrium state of starburst galaxies may result in short τ_{dep} due to the contribution of the $\tau_\star/\tau_{\text{e,sf}}$ term in Equation (9).

Our framework also predicts the dependence of depletion times and KSR shape on metallicity. Gas must be shielded by a certain column density in order to become cold and molecular. This column density has a corresponding number density at which such a transition occurs, as can be seen in the phase

diagrams in Figure 6, that show the sharp change from warm, transonic phase (yellow) to cold, supersonic phase (blue) at $n \sim 10 \text{ cm}^{-3}$. At lower metallicities, both the characteristic number density and column density of the transition increase, leading to the decrease of f_{H_2} , f_{sf} and τ_\star . Thus, the overall gas depletion time, τ_{dep} , increases. The mechanism of $f_{\text{sf,H}_2}$ regulation by feedback-driven turbulence discussed in Section 4.4, however, should operate regardless of the gas metallicity. Thus, we expect the KSR for molecular gas to remain linear at low metallicity. Although we also expect its normalization to be approximately independent of gas metallicity, a weak dependence is possible due to the changing properties of star-forming regions with metallicity.

The higher characteristic density of the transition at lower metallicity also results in the shift of the turnover in the KSR for total gas to higher surface densities. This shift is qualitatively similar to that predicted by the Gnedin & Kravtsov (2011) models, where star formation is tied to molecular gas. We have confirmed this explicitly by re-simulating our model galaxy at a lower metallicity and will present these results in a forthcoming paper.

5.2. Implications for galaxy formation simulations

Recent studies show that in simulations with strong feedback the galaxy-scale star formation rate, and hence its global depletion time, is insensitive to the local star formation efficiency (e.g., Dobbs et al. 2011; Hopkins et al. 2013, 2017; Agertz et al. 2013; Agertz & Kravtsov 2015; Benincasa et al. 2016; Orr et al. 2017). This behavior is thought to be due to “self-regulation” of star formation by feedback (e.g., Dobbs et al. 2011).

Our framework naturally explains the physical mechanism of such self-regulation. Equation (9) accounts for feedback via the term proportional to the mass loading factor, ξ , defined as the proportionality factor between the rate of star-forming gas dispersal by feedback and star formation rate. When feedback is sufficiently strong so that this term dominates, the depletion time is given by $\tau_{\text{dep}} \approx \xi\tau_+$, where τ_+ is the time scale of star-forming gas supply from the ISM. Thus, in this regime, the star formation rate of a galaxy is $\dot{M}_\star = M_g/\tau_{\text{dep}} \sim M_g/(\xi\tau_+)$. Physically, τ_+ is not related to the local star formation efficiency, while ξ is the ratio of the star-forming gas depletion time, $\tau_\star = \langle \epsilon_{\text{ff}}/t_{\text{ff}} \rangle_{\text{sf}}^{-1}$, and the time scale with which feedback disperses star-forming gas, $\tau_{\text{-fb}}$ (see Section 2). Time scales τ_\star and $\tau_{\text{-fb}}$ are proportional to each other, because the rate of gas removal from star-forming regions is proportional to the rate of energy and momentum injection by feedback, which, in turn, is proportional to the star formation rate: $M_{\text{sf}}/\tau_{\text{-fb}} = \xi\dot{M}_\star = \xi M_{\text{sf}}/\tau_\star$. Thus, the global star-formation rate in this regime, $\dot{M}_\star \sim M_g/(\xi\tau_+)$, does not depend on the local depletion time and thus local star formation efficiency. At the same time, \dot{M}_\star is inversely proportional to the strength of feedback, ξ , as observed in simulations with self-regulation (e.g., Orr et al. 2017; Hopkins et al. 2017).

Note that for a given strength of feedback, the regime of self-regulation exists only for a certain range of ϵ_{ff} and τ_\star . For sufficiently low ϵ_{ff} (long τ_\star), the second term in the sum in Equation (9), i.e. τ_\star , will dominate and the global depletion time will scale with the local star formation efficiency as $\tau_{\text{dep}} \sim \tau_\star \propto \epsilon_{\text{ff}}^{-1}$. Indeed, we have checked that when feedback parameters and star formation threshold in our simulations are fixed, the global depletion time is insensitive to the variation of local efficiency for $\epsilon_{\text{ff}} > 1\%$, but scales as $\tau_{\text{dep}} \propto \epsilon_{\text{ff}}^{-1}$ when

$\epsilon_{\text{ff}} < 1\%$.

The critical value of ϵ_{ff} , above which τ_{dep} becomes insensitive to ϵ_{ff} , depends on the relative contribution of the τ_* term in the sum of Equation (9), and thus depends on the factors that control the first term in the sum, in particular feedback strength ξ . Dependence of the critical ϵ_{ff} on feedback strength explains the results of Agertz et al. (2013) and Agertz & Kravtsov (2015), who found that the normalization of the KSR, i.e., τ_{dep}^{-1} , scales with ϵ_{ff} in simulations without feedback but is similar for $\epsilon_{\text{ff}} = 1\%$ and 10% when feedback is strong.

The weak sensitivity of the SFR to the value of ϵ_{ff} in the regime of strong feedback does not mean that this value is not important. For example, the mass fraction of star-forming gas in this regime scales inversely with ϵ_{ff} : $f_{\text{sf}} \equiv M_{\text{sf}}/M_{\text{g}} = \tau_*/\tau_{\text{dep}} \propto \epsilon_{\text{ff}}^{-1}$. Thus, an incorrect ϵ_{ff} will result in an incorrect mass fraction and an incorrect spatial distribution of star-forming gas.

The mass fraction of star-forming gas and its distribution is also a non-trivial function of the feedback strength and the specific mix of processes that define it (e.g., Butler et al. 2017). Stronger feedback shortens the time that gas spends in the star-forming state, t_{sf} , and, therefore, decreases the mass fraction of star-forming gas: $f_{\text{sf}} \equiv M_{\text{sf}}/M_{\text{g}} \sim t_{\text{sf}}/(t_{\text{nsf}} + t_{\text{sf}})$. Besides, strong feedback shapes the overall gas PDF and may increase time scales t_{nsf} , which also results in a decrease of f_{sf} . This happens, for example, when a gaseous disk is stabilized by a pressure corresponding to a slowly dissipating energy directly injected by feedback (e.g., Agertz et al. 2013; Benincasa et al. 2016).

Finally, t_{nsf} , t_{sf} and f_{sf} depend on the overall adopted definition of star-forming gas. Usually, the boundary between star-forming and non-star-forming gas is established by a set of thresholds in various gas properties, such as gas density, molecular fraction, virial parameter α_{vir} , etc. Our results indicate that these thresholds should be carefully chosen because if thresholds grossly misidentify the star-forming gas, the values of ϵ_{ff} and feedback strength may need to compensate for the wrong choice to get reasonable t_{sf} and f_{sf} values. It is not yet clear whether such compensation is possible in general but, in any case, wrong thresholds may drive the ϵ_{ff} and feedback parameters to incorrect values.

In addition, the choice of the thresholds defining star-forming gas indirectly affects the efficiency of feedback. When more gas is designated to be star-forming for a given fixed star formation rate, the feedback mass loading factor, ξ , will have to be larger, i.e., feedback has to be stronger. The specific choice of the thresholds matters as well. For example, when star-forming gas is defined using a density threshold, n_{sf} , feedback has to drive star-forming gas to lower densities, $n < n_{\text{sf}}$, in order to shut down star formation. If star-forming gas is defined using a threshold in the virial parameter instead, α_{vir} can be increased to values larger than the threshold very quickly by injecting thermal or turbulent energy without changing the gas density significantly.

Thus, the framework presented in this paper implies that to get the value of f_{sf} and depletion time, $\tau_{\text{dep}} = \tau_*/f_{\text{sf}}$, and the distribution of star-forming gas correctly, the overall definition of the star-forming gas, its star formation efficiency, and the strength of stellar feedback are all important and should all be modeled carefully. Ideally, the modeling choices should be based on solid physical ground or subgrid models calibrated on higher resolution simulations. For example, recent studies showed that local ϵ_{ff} can be modeled using the results of high-

resolution simulations of turbulent star-forming gas (Padoan et al. 2012, 2017; Federrath 2015) and a subgrid model for turbulence calibrated on turbulence simulations (e.g., Braun et al. 2014; Braun & Schmidt 2015; Semenov et al. 2016; Li et al. 2017).

Interestingly, the results presented in Section 4.4 indicate that feedback can break the direct connection between the small- and large-scale relations between gas density and SFR. Specifically, in our simulations it is assumed that $\dot{\rho}_* \propto \rho^{1.5}$ on the scales of individual cells. However, as can be seen in Figures 3 and 9, on kiloparsec scales the relation between the surface density of molecular gas and star formation rate is almost linear. This result provides a counter-example to the arguments that in simulations the slope of the Kennicutt-Schmidt relation on kiloparsec scales simply reflects the assumed density dependence of the local SFR on small scales (Schaye & Dalla Vecchia 2008; Gnedin et al. 2014). Our analysis shows that the linear relation arises because only a fraction of cold, dense gas is forming stars and its density PDF does not scale self-similarly with the large-scale surface density of molecular gas, Σ_{H_2} . Variation in covering fraction allows Σ_{H_2} to vary significantly, while the average density of star-forming gas and the corresponding depletion time vary only weakly. In addition, self-regulation by feedback ties the fraction of molecular gas that is forming stars and the depletion time of star-forming gas, so that their trends with Σ_{H_2} are similar. These trends cancel out resulting in an almost constant $\tau_{\text{dep,H}_2}$ and linear $\dot{\Sigma}_* - \Sigma_{\text{H}_2}$ relation.

The emergence of the large-scale KSR via non-trivial non-linear effects of the star formation-feedback loop motivates efforts to model such processes in high-resolution simulations rather than tuning the star formation prescription to produce a particular large-scale relation.

Our model also sheds some light on the importance of the so-called “early feedback” — a collective name for the energy and momentum injection by young stars during the first 3 Myrs in the life of a stellar population, before first supernovae explode. The time lag between the formation of stellar particles and the onset of feedback is important when τ_* is comparable to the lag. In this case, a substantial fraction of the gas mass can be converted into stars in the first 3 Myr before supernova feedback can limit star formation. When τ_* is long, the global depletion time becomes less sensitive to the presence or absence of stellar feedback during the first 3 Myr of the star-forming stage.

6. SUMMARY AND CONCLUSIONS

We presented a simple and intuitive model that elucidates why gas depletion times in galaxies are long compared to the time scales of the processes driving the evolution of the interstellar medium. We show that the depletion time is long not because a bottleneck in the gas supply imposes a long evolution time scale, but because only a small fraction of gas mass is converted into stars during a single star-forming stage in the evolution of a gas parcel. This fraction is small due to both the short duration of the star-forming stage, as dynamical processes and stellar feedback efficiently disperse star-forming regions, and the low intrinsic star formation efficiency of dense molecular gas. A gas parcel thus must go through many cycles transitioning between non-star-forming and star-forming states before it can convert its gas into stars. Hence, even though the duration of each cycle can be short the global depletion time is long because the number of cycles is

large.

Furthermore, the difference between the global and local depletion times of molecular gas in our model arises because not all of the molecular gas is actively forming stars. Non-star-forming molecular gas appears naturally if local star formation efficiency is a strong function of the virial parameter of a region, while the molecular fraction of gas is set by its ability to shield against FUV radiation and is a function of mainly gas number density and metallicity.

We illustrate our model using the results of an isolated L_* -sized disk galaxy simulation that reproduces the observed Kennicutt-Schmidt relation for molecular and atomic gas. We discuss the predictions of our model for the dependence of the global depletion time on properties of observed galaxies and on the parameters of star formation and feedback recipes in galaxy simulations. In particular, our model explains the weak sensitivity of the global star formation rate to the assumed local star formation efficiency reported in several recent numerical studies and the physics of this “self-regulation” (see Sections 2 and 5.2).

Additional results and conclusions can be summarized as follows.

1. Analysis of our simulation shows that the properties of gas parcels in the ISM evolve on time scales of $\sim 10 - 100$ Myr under the influence of compression by spiral arms, ISM turbulence, and SNe-driven shocks. The relative importance of these processes varies with galactocentric radius, R , and average surface density. At $R \gtrsim 5$ kpc the evolution from warm, diffuse state to dense, cold phase is driven mainly by compression in spiral arms, while SNe-driven shocks and large-scale ISM turbulence dominate at smaller radii.
2. During an evolutionary cycle, gas spends most of the time in the non-star-forming state, $t_{\text{nsf}} > t_{\text{sf}}$, whereas the time spent in the star-forming state, t_{sf} , is limited by stellar feedback and dynamical processes to $t_{\text{sf}} \sim 5 - 15$ Myr. We find that the median t_{nsf} varies with gas surface density as $t_{\text{nsf}} \propto \Sigma_g^{-0.5}$.
3. On the resolution scale of our simulation, 40 pc, the typical range of densities in star-forming regions is limited to $n \sim 10 - 10^3 \text{ cm}^{-3}$ by interstellar FUV background and stellar feedback. We find that the resulting depletion times of star-forming gas $\tau_* \sim 300 - 500$ Myr are consistent with the depletion times estimated for observed GMCs on these scales and exhibit only weak trends with the surface densities of total and molecular gas.
4. The distribution of depletion times and lifetimes of star-forming regions in our simulations imply that a typical

gas parcel has to undergo 5 – 100 cycles transitioning between non-star-forming and star-forming states before converting its mass into stars.

5. On kiloparsec scales our simulation produces a nearly linear relation between the surface density of H_2 and surface density of star formation rate, i.e., the molecular Kennicutt-Schmidt relation, even though a non-linear local relation, $\dot{\rho}_* \propto \rho^{1.5}$, is adopted for star-forming gas in simulation cells. We show that the linear relation emerges due to stellar feedback, which shapes the gas density PDF making it non-self-similar and establishes a correlation between local depletion time of star-forming gas and the fraction of molecular gas that is in the star-forming state.

The model for the global depletion time scale presented in this paper is a generic framework that can be applied not only to galaxies as a whole, but also to individual ISM patches with size ranging from \sim kiloparsec to a typical size of star-forming regions, ~ 10 pc. It can also be used to predict and interpret trends of gas depletion time with the ISM properties and redshift.

As a final comment, we note that in the context of galaxy evolution over cosmological time scales the actual gas depletion time is often considered to be unimportant, as the total SFR predicted in galaxy evolution models was shown to be determined by the rates of gas accretion and gas loss in galactic winds (e.g., Bouché et al. 2010; Davé et al. 2012; Lilly et al. 2013). However, this is only true at $z \lesssim 5 - 6$. At higher z , when the age of the Universe is $\lesssim 1$ Gyr, the gas depletion time scale becomes comparable to the cosmological evolution time scale and will therefore play an important role in controlling the SFR during the early stages of galaxies evolution (e.g., Peng & Maiolino 2014; Dekel & Mandelker 2014). The framework for modeling gas depletion time presented in this paper thus opens a way to refine theoretical models of galaxy formation in this regime, particularly important in the upcoming era of the JWST.

We thank Cameron Liang, Claude-André Faucher-Giguère, Robert Feldmann, Romain Teyssier, Simon Lilly, and Marcella Carollo for useful discussions. We are also grateful to Oscar Agertz, Camille Avestruz, Benedikt Diemer, Oleg Gnedin, Hui Li, and Philip Mansfield whose valuable comments and suggestions helped to improve our paper. This work was supported by a NASA ATP grant NNH12ZDA001N, NSF grant AST-1412107, and by the Kavli Institute for Cosmological Physics at the University of Chicago through grant PHY-1125897 and an endowment from the Kavli Foundation and its founder Fred Kavli. The simulation presented in this paper have been carried out using the Midway cluster at the University of Chicago Research Computing Center, which we acknowledge for support.

REFERENCES

- Agertz, O., & Kravtsov, A. V. 2015, *ApJ*, 804, 18
 Agertz, O., Kravtsov, A. V., Leitner, S. N., & Gnedin, N. Y. 2013, *ApJ*, 770, 25
 Benincasa, S. M., Wadsley, J., Couchman, H. M. P., & Keller, B. W. 2016, *MNRAS*, 462, 3053
 Bigiel, F., Leroy, A., Walter, F., et al. 2010, *AJ*, 140, 1194
 —. 2008, *AJ*, 136, 2846
 Bigiel, F., Leroy, A. K., Walter, F., et al. 2011, *ApJ*, 730, L13
 Bissantz, N., Englmaier, P., & Gerhard, O. 2003, *MNRAS*, 340, 949
 Bouché, N., Cresci, G., Davies, R., et al. 2007, *ApJ*, 671, 303
 Bouché, N., Dekel, A., Genzel, R., et al. 2010, *ApJ*, 718, 1001
 Braun, H., & Schmidt, W. 2015, *MNRAS*, 454, 1545
 Braun, H., Schmidt, W., Niemeyer, J. C., & Almgren, A. S. 2014, *MNRAS*, 442, 3407
 Braun, R. 2012, *ApJ*, 749, 87
 Butler, M. J., Tan, J. C., Teyssier, R., et al. 2017, *ApJ* submitted (arXiv:1703.04509), arXiv:1703.04509
 Chabrier, G. 2003, *PASP*, 115, 763
 Christensen, C., Quinn, T., Governato, F., et al. 2012, *MNRAS*, 425, 3058
 Daddi, E., Elbaz, D., Walter, F., et al. 2010, *ApJ*, 714, L118

- Davé, R., Finlator, K., & Oppenheimer, B. D. 2012, *MNRAS*, 421, 98
- Davis, B. L., Kennefick, D., Kennefick, J., et al. 2015, *ApJ*, 802, L13
- Dekel, A., & Mandelker, N. 2014, *MNRAS*, 444, 2071
- Dobbs, C. L., Burkert, A., & Pringle, J. E. 2011, *MNRAS*, 413, 2935
- Dobbs, C. L., Pringle, J. E., & Burkert, A. 2012, *MNRAS*, 425, 2157
- Dobbs, C. L., Pringle, J. E., & Duarte-Cabral, A. 2015, *MNRAS*, 446, 3608
- Elmegreen, B. G. 2002, *ApJ*, 577, 206
- . 2015, *ApJ*, 814, L30
- Evans, II, N. J., Heiderman, A., & Vutisalchavakul, N. 2014, *ApJ*, 782, 114
- Evans, II, N. J., Dunham, M. M., Jørgensen, J. K., et al. 2009, *ApJS*, 181, 321
- Faucher-Giguère, C.-A., Quataert, E., & Hopkins, P. F. 2013, *MNRAS*, 433, 1970
- Federrath, C. 2013, *MNRAS*, 436, 3167
- Federrath, C. 2015, *MNRAS*, 450, 4035
- Feldmann, R., Gnedin, N. Y., & Kravtsov, A. V. 2011, *ApJ*, 732, 115
- Froebich, D., & Rowles, J. 2010, *MNRAS*, 406, 1350
- Gavagnin, E., Bleuler, A., Rosdahl, J., & Teyssier, R. 2017, *ArXiv e-prints*, arXiv:1701.07982
- Gentry, E. S., Krumholz, M. R., Dekel, A., & Madau, P. 2017, *MNRAS*, 465, 2471
- Genzel, R., Tacconi, L. J., Gracia-Carpio, J., et al. 2010, *MNRAS*, 407, 2091
- Gnedin, N. Y., & Hollon, N. 2012, *ApJS*, 202, 13
- Gnedin, N. Y., & Kravtsov, A. V. 2011, *ApJ*, 728, 88
- Gnedin, N. Y., Tasker, E. J., & Fujimoto, Y. 2014, *ApJ*, 787, L7
- Gnedin, N. Y., Tassis, K., & Kravtsov, A. V. 2009, *ApJ*, 697, 55
- Gutermuth, R. A., Pipher, J. L., Megeath, S. T., et al. 2011, *ApJ*, 739, 84
- Hayward, C. C., & Hopkins, P. F. 2017, *MNRAS*, 465, 1682
- Heiderman, A., Evans, II, N. J., Allen, L. E., Huard, T., & Heyer, M. 2010, *ApJ*, 723, 1019
- Heiles, C., & Troland, T. H. 2003, *ApJ*, 586, 1067
- Hernquist, L. 1990, *ApJ*, 356, 359
- Heyer, M., Gutermuth, R., Urquhart, J. S., et al. 2016, *A&A*, 588, A29
- Hopkins, P. F., Narayanan, D., & Murray, N. 2013, *MNRAS*, 432, 2647
- Hopkins, P. F., Wetzell, A., Keres, D., et al. 2017, *ArXiv e-prints*, arXiv:1702.06148
- Kawamura, A., Mizuno, Y., Minamidani, T., et al. 2009, *ApJS*, 184, 1
- Kennicutt, R. C., & Evans, N. J. 2012, *ARA&A*, 50, 531
- Kennicutt, Jr., R. C. 1989, *ApJ*, 344, 685
- . 1998, *ApJ*, 498, 541
- Kim, J.-h., Agertz, O., Teyssier, R., et al. 2016, *ApJ*, 833, 202
- Kravtsov, A. V. 1999, PhD thesis, NEW MEXICO STATE UNIVERSITY
- Kravtsov, A. V., Klypin, A., & Hoffman, Y. 2002, *ApJ*, 571, 563
- Kruijssen, J. M. D., & Longmore, S. N. 2014, *MNRAS*, 439, 3239
- Krumholz, M. R., & Burkert, B. 2016, *MNRAS*, 458, 1671
- Krumholz, M. R., Dekel, A., & McKee, C. F. 2012, *ApJ*, 745, 69
- Krumholz, M. R., & McKee, C. F. 2005, *ApJ*, 630, 250
- Krumholz, M. R., McKee, C. F., & Tumlinson, J. 2008, *ApJ*, 689, 865
- . 2009a, *ApJ*, 693, 216
- . 2009b, *ApJ*, 699, 850
- Krumholz, M. R., & Tan, J. C. 2007, *ApJ*, 654, 304
- Kuhlen, M., Krumholz, M. R., Madau, P., Smith, B. D., & Wise, J. 2012, *ApJ*, 749, 36
- Lada, C. J., Forbrich, J., Lombardi, M., & Alves, J. F. 2012, *ApJ*, 745, 190
- Lada, C. J., Lombardi, M., & Alves, J. F. 2010, *ApJ*, 724, 687
- Lee, E. J., Miville-Deschênes, M.-A., & Murray, N. W. 2016, *ApJ*, 833, 229
- Leitner, S. N., & Kravtsov, A. V. 2011, *ApJ*, 734, 48
- Leroy, A. K., Walter, F., Brinks, E., et al. 2008, *AJ*, 136, 2782
- Li, H., Gnedin, O. Y., Gnedin, N. Y., et al. 2017, *ApJ*, 834, 69
- Li, Y., Mac Low, M.-M., & Klessen, R. S. 2005, *ApJ*, 620, L19
- Lilly, S. J., Carollo, C. M., Pipino, A., Renzini, A., & Peng, Y. 2013, *ApJ*, 772, 119
- Mac Low, M.-M., Klessen, R. S., Burkert, A., & Smith, M. D. 1998, *Physical Review Letters*, 80, 2754
- Madore, B. F., van den Bergh, S., & Rogstad, D. H. 1974, *ApJ*, 191, 317
- Martizzi, D., Faucher-Giguère, C.-A., & Quataert, E. 2015, *MNRAS*, 450, 504
- McKee, C. F., & Krumholz, M. R. 2010, *ApJ*, 709, 308
- Misiriotis, A., Xilouris, E. M., Papamastorakis, J., Boumis, P., & Goudis, C. D. 2006, *A&A*, 459, 113
- Miville-Deschênes, M.-A., Murray, N., & Lee, E. J. 2017, *ApJ*, 834, 57
- Murray, N. 2011, *ApJ*, 729, 133
- Orr, M., Hayward, C., Hopkins, P., et al. 2017, *MNRAS submitted* (arXiv:1701.01788), arXiv:1701.01788
- Ostriker, E. C., McKee, C. F., & Leroy, A. K. 2010, *ApJ*, 721, 975
- Ostriker, E. C., & Shetty, R. 2011, *ApJ*, 731, 41
- Padoan, P., Federrath, C., Chabrier, G., et al. 2014, *Protostars and Planets VI*, 77
- Padoan, P., Haugbølle, T., & Nordlund, Å. 2012, *ApJ*, 759, L27
- Padoan, P., Haugbølle, T., Nordlund, Å., & Frimann, S. 2017, *ApJ submitted* (arXiv:1702.07270), arXiv:1702.07270
- Peng, Y.-j., & Maiolino, R. 2014, *MNRAS*, 443, 3643
- Pineda, J. L., Langer, W. D., Velusamy, T., & Goldsmith, P. F. 2013, *A&A*, 554, A103
- Rahmati, A., Pawlik, A. H., Raičević, M., & Schaye, J. 2013, *MNRAS*, 430, 2427
- Rebolledo, D., Wong, T., Xue, R., et al. 2015, *ApJ*, 808, 99
- Renaud, F., Kraljic, K., & Bournaud, F. 2012, *ApJ*, 760, L16
- Robertson, B., & Goldreich, P. 2012, *ApJ*, 750, L31
- Robertson, B. E., & Kravtsov, A. V. 2008, *ApJ*, 680, 1083
- Rudd, D. H., Zentner, A. R., & Kravtsov, A. V. 2008, *ApJ*, 672, 19
- Safrank-Shrader, C., Krumholz, M. R., Kim, C.-G., et al. 2017, *MNRAS*, 465, 885
- Saitoh, T. R., Daisaka, H., Kokubo, E., et al. 2008, *PASJ*, 60, 667
- Salim, D. M., Federrath, C., & Kewley, L. J. 2015, *ApJ*, 806, L36
- Sanduleak, N. 1969, *AJ*, 74, 47
- Schaye, J., & Dalla Vecchia, C. 2008, *MNRAS*, 383, 1210
- Schmidt, M. 1959, *ApJ*, 129, 243
- Schmidt, W., Almgren, A. S., Brauer, H., et al. 2014, *MNRAS*, 440, 3051
- Schruba, A., Leroy, A. K., Walter, F., Sandstrom, K., & Rosolowsky, E. 2010, *ApJ*, 722, 1699
- Schruba, A., Leroy, A. K., Kruijssen, J. M. D., et al. 2017, *ApJ*, 835, 278
- Semenov, V. A., Kravtsov, A. V., & Gnedin, N. Y. 2016, *ApJ*, 826, 200
- Silk, J. 1997, *ApJ*, 481, 703
- Silk, J., & Norman, C. 2009, *ApJ*, 700, 262
- Sofue, Y. 2017, *ArXiv e-prints*, arXiv:1703.05565
- Stecher, T. P., & Williams, D. A. 1967, *ApJ*, 149, L29
- Tacconi, L. J., Genzel, R., Saintonge, A., et al. 2017, *ArXiv e-prints*, arXiv:1702.01140
- Tan, J. C. 2000, *ApJ*, 536, 173
- Toomre, A. 1964, *ApJ*, 139, 1217
- Vutisalchavakul, N., Evans, II, N. J., & Heyer, M. 2016, *ApJ*, 831, 73
- Wolfire, M. G., McKee, C. F., Hollenbach, D., & Tielens, A. G. G. M. 2003, *ApJ*, 587, 278
- Wong, T., & Blitz, L. 2002, *ApJ*, 569, 157
- Wyse, R. F. G., & Silk, J. 1989, *ApJ*, 339, 700
- Zuckerman, B., & Evans, II, N. J. 1974, *ApJ*, 192, L149
- Zuckerman, B., & Palmer, P. 1974, *ARA&A*, 12, 279